

Frequency-Guided Posterior Sampling for Diffusion-Based Image Restoration

Darshan Thaker
University of Pennsylvania
dbthaker@seas.upenn.edu

Abhishek Goyal
University of Pennsylvania
abhi2358@seas.upenn.edu

René Vidal
University of Pennsylvania
vidalr@seas.upenn.edu

Abstract

Image restoration aims to recover high-quality images from degraded observations. When the degradation process is known, the recovery problem can be formulated as an inverse problem, and in a Bayesian context, the goal is to sample a clean reconstruction given the degraded observation. Recently, modern pretrained diffusion models have been used for image restoration by modifying their sampling procedure to account for the degradation process. However, these methods often rely on certain approximations that can lead to significant errors and compromised sample quality. In this paper, we provide the first rigorous analysis of this approximation error for linear inverse problems under distributional assumptions on the space of natural images, demonstrating cases where previous works can fail dramatically. Motivated by our theoretical insights, we propose a simple modification to existing diffusion-based restoration methods. Our approach introduces a time-varying low-pass filter in the frequency domain of the measurements, progressively incorporating higher frequencies during the restoration process. We develop an adaptive curriculum for this frequency schedule based on the underlying data distribution. Our method significantly improves performance on challenging image restoration tasks including motion deblurring and image dehazing.

1. Introduction

Image restoration is a fundamental problem in computer vision whose goal is to recover high-quality images from degraded observations. Many image restoration problems can be cast as inverse problems, where the task is to recover an underlying signal $\mathbf{x}_0 \in \mathbb{R}^n$ from noisy measurements $\mathbf{y} \in \mathbb{R}^m$ that are obtained from \mathbf{x}_0 via

$$\mathbf{y} = \mathcal{A}(\mathbf{x}_0) + \mathbf{z}. \quad (1)$$

In the above, $\mathcal{A} : \mathbb{R}^n \rightarrow \mathbb{R}^m$ denotes the forward operator, which we assume to be known, and $\mathbf{z} \in \mathbb{R}^m$ is additive Gaussian noise.

In most applications, recovering \mathbf{x}_0 is difficult because

the forward operator is a many-to-one mapping. To address this challenge, researchers incorporate prior knowledge about \mathbf{x}_0 , including sparsity [5, 16], low-rank structure [4, 6], total variation [31], or deep generative priors [3, 29]. One way of enforcing this knowledge is by solving a regularized optimization problem where the objective is to find an \mathbf{x}_0 that maximizes the likelihood under the chosen prior model while satisfying the constraint $\mathbf{y} = \mathcal{A}(\mathbf{x}_0)$. Another approach is to follow the Bayesian viewpoint where instead of recovering an exact \mathbf{x}_0 , we sample from $p(\mathbf{x} | \mathbf{y})$ where Equation (1) is the model for $p(\mathbf{y} | \mathbf{x}_0)$ [36]. The advantage of this interpretation is that we can draw multiple plausible samples. In image restoration tasks, the diversity of samples can help the user pick a visually appealing reconstruction.

Recently, diffusion models [20, 34] have shown tremendous success in modeling complex probability distributions, allowing one to generate diverse and visually coherent samples in image, video, and audio tasks [14, 21, 25]. During training, diffusion models learn to reverse a gradual noising process that transforms data \mathbf{x}_0 to pure noise \mathbf{x}_T over T steps, where \mathbf{x}_t denotes an intermediate step of the reverse diffusion process. At test time, they generate samples by iteratively denoising random noise, progressively refining it into coherent data. Naturally, these models can also be used to develop samplers for $p(\mathbf{x} | \mathbf{y})$ in inverse problem settings. However, while one can train a problem-specific diffusion model to sample directly from $p(\mathbf{x} | \mathbf{y})$ [32], this requires training new diffusion models for every inverse problem, limiting the practical use of such approaches.

A popular approach which does not require training a new diffusion model for $p(\mathbf{x} | \mathbf{y})$ is to modify the sampling process of a pretrained unconditional diffusion model so that it produces samples that are consistent with the given measurement \mathbf{y} [9, 24, 33, 35, 40]. These methods are based on decomposing the conditional score function $\nabla_{\mathbf{x}_t} \log p(\mathbf{x}_t | \mathbf{y})$ as $\nabla_{\mathbf{x}_t} \log p(\mathbf{x}_t) + \nabla_{\mathbf{x}_t} \log p(\mathbf{y} | \mathbf{x}_t)$ using the Bayes rule. While the first term is learned by a pretrained unconditional diffusion model, the second term is analytically intractable in general because \mathbf{x}_t is the result of a complex denoising process. Thus, in practice, we use approximations for this term, typically by first computing

arXiv:2411.15295v1 [eess.IV] 22 Nov 2024

$\mu_{0|t} = \mathbb{E}[\mathbf{x}_0 | \mathbf{x}_t]$ using the learned diffusion model, known as the Tweedie estimate [17], and following the gradient of a loss that measures the deviation between $\mathcal{A}(\mu_{0|t})$ and \mathbf{y} . While intuitive, the approximation error from the Tweedie estimate is difficult to control. Previous work has attempted to address this by designing heuristics that ensure that the modifications to \mathbf{x}_t respect the intermediate data manifold learned by the diffusion model. However, these approaches make strong assumptions about the data manifold’s structure, such as linearity, or require that $\mu_{0|t}$ remains on the clean data manifold throughout all iterations [10, 41].

Our work aims to better understand and control this approximation error by analyzing images in the frequency domain. Our main contributions are:

1. For linear inverse problems, for the first time in the literature, we exactly characterize the approximation gap between $\nabla_{\mathbf{x}_t} \log p(\mathbf{y} | \mathbf{x}_t)$ and commonly used approximations under distributional assumptions on the data. Further, exploiting the frequency distribution of natural images, we give precise examples of forward operators that can result in very large approximation gaps.
2. Our analysis guides us in developing a new unsupervised diffusion-based image restoration algorithm, denoted as **F**requency **G**uided **P**osterior **S**ampling (FGPS). To handle the intricate relationship between the frequency characteristics of the data and the forward operator, we apply a time-varying low-pass filter to \mathbf{y} in its frequency domain which progressively includes higher frequency ranges during the reverse diffusion process.
3. We develop a data-dependent curriculum for the low-pass filters. While being easy to implement, our algorithm leads to a significant boost in performance on challenging linear and nonlinear image restoration problems, such as motion deblurring and image dehazing.

2. Background

2.1. Diffusion Models

Diffusion models are a class of score-based generative models that sample from a given data distribution by learning to reverse a gradual noising process [20, 34]. This noising process, known as the forward process, is represented in continuous time as an Itô Stochastic Differential Equation (SDE) for $t \in [0, 1]$

$$d\mathbf{x}_t = -\frac{1}{2}\beta(t)\mathbf{x}_t dt + \sqrt{\beta(t)}d\mathbf{w}_t. \quad (2)$$

The SDE is characterized by its drift coefficient $-\frac{1}{2}\beta(t)$ and diffusion coefficient $\sqrt{\beta(t)}$, with \mathbf{w}_t representing the standard Wiener process over the interval $[0, 1]$. The initial condition of this SDE is a datapoint $\mathbf{x}_0 \sim p(\mathbf{x})$. The drift and diffusion coefficients are chosen such that \mathbf{x}_t goes

from the clean data distribution at $t = 0$ to pure noise $\mathbf{x}_1 \sim \mathcal{N}(\mathbf{0}, \mathbf{I})$ at $t = 1$. A special case is known as the Variance-Preserving SDE (VP-SDE), where we can write the transition density $p_t(\mathbf{x}_t | \mathbf{x}_0)$ as

$$p(\mathbf{x}_t | \mathbf{x}_0) = \mathcal{N}(\sqrt{\bar{\alpha}_t}\mathbf{x}_0, (1 - \bar{\alpha}_t)\mathbf{I}), \quad (3)$$

for $\bar{\alpha}_t = e^{\int_0^t \beta(s) ds}$ [20].

The reverse process aims to remove the noise from \mathbf{x}_1 and draw a sample from \mathbf{x}_0 following the reverse-time SDE

$$d\mathbf{x}_t = \left[-\frac{\beta(t)}{2}\mathbf{x}_t - \beta(t)\nabla_{\mathbf{x}_t} \log p_t(\mathbf{x}_t) \right] dt + \sqrt{\beta(t)}d\bar{\mathbf{w}}_t, \quad (4)$$

where t and the new Wiener process $\bar{\mathbf{w}}_t$ both run in reverse. A seminal result of Anderson gives that this reverse process has the same probability distribution as the forward process for every t [1]. In order to estimate the time-dependent score function $\nabla_{\mathbf{x}_t} \log p_t(\mathbf{x}_t)$, diffusion models use the denoising score matching technique to train a neural network that approximates the score function [39]. Sampling from $p(\mathbf{x})$ is performed by solving a discrete-time version of Equation (4) over T steps, where $\mathbf{x}_T \sim \mathcal{N}(\mathbf{0}, \mathbf{I})$ [20, 35].

2.2. Posterior Sampling

In inverse problems, we are given measurements \mathbf{y} as in Equation (1), and the goal is to recover the underlying clean \mathbf{x}_0 given \mathbf{y} . Because \mathcal{A} is not invertible in general, the inverse problem can be highly ill-posed, and assumptions on the data are needed to make the problem tractable.

A popular Bayesian strategy to solve the problem is to develop samplers for $p(\mathbf{x} | \mathbf{y})$ assuming we have a prior for $p(\mathbf{x})$ modeled by a pretrained generative model such as a diffusion model. For instance we can extend Equation (4) to sample from $p(\mathbf{x} | \mathbf{y})$ by using a conditional score function

$$d\mathbf{x}_t = \left[-\frac{\beta(t)}{2}\mathbf{x}_t - \beta(t)\nabla_{\mathbf{x}_t} \log p_t(\mathbf{x}_t | \mathbf{y}) \right] dt + \sqrt{\beta(t)}d\bar{\mathbf{w}}_t. \quad (5)$$

While one could train a conditional diffusion model to approximate the conditional score, this would require retraining models for every inverse problem we wish to solve [32]. Instead, we can use Bayes rule to write the conditional score as

$$\nabla_{\mathbf{x}_t} \log p(\mathbf{x}_t | \mathbf{y}) = \underbrace{\nabla_{\mathbf{x}_t} \log p(\mathbf{x}_t)}_{\text{unconditional score}} + \underbrace{\nabla_{\mathbf{x}_t} \log p(\mathbf{y} | \mathbf{x}_t)}_{\text{noisy likelihood score}} \quad (6)$$

While a pretrained diffusion model effectively approximates the unconditional score, the noisy likelihood score remains intractable due to its factorization

$$p(\mathbf{y} | \mathbf{x}_t) = \int p(\mathbf{y} | \mathbf{x}_0)p(\mathbf{x}_0 | \mathbf{x}_t)d\mathbf{x}_0, \quad (7)$$

where $p(\mathbf{x}_0 | \mathbf{x}_t)$ represents the complex distribution of denoised estimates of \mathbf{x}_t . Even though $p(\mathbf{x}_0 | \mathbf{x}_t)$ can be complex, the Tweedie’s estimate gives us the posterior mean $\boldsymbol{\mu}_{0|t} = \mathbb{E}[\mathbf{x}_0 | \mathbf{x}_t]$ as a function of the unconditional score function [17] (refer to Appendix A for more background). Thus, some unsupervised methods approximate $p(\mathbf{x}_0 | \mathbf{x}_t)$ using $\boldsymbol{\mu}_{0|t}$, for example as a Dirac delta around $\boldsymbol{\mu}_{0|t}$ [9] or an isotropic Gaussian distribution with mean $\boldsymbol{\mu}_{0|t}$ [33]. This results in tractable approximations for the conditional score $\nabla_{\mathbf{x}_t} \log p(\mathbf{x}_t | \mathbf{y})$, but introduces a potentially large approximation error. In this work, we quantify this approximation gap exactly under distributional assumptions on \mathbf{x}_0 , and use our insights to develop a simple modification that reduces the approximation gap significantly.

2.3. Signal Processing Basics

Our method relies on the frequency decomposition of natural images, so in this section, we review the terminology used for the remainder of the paper. The Discrete Fourier Transform (DFT) of a finite signal $\mathbf{x} \in \mathbb{R}^n$, denoted as $\mathcal{F}(\mathbf{x})$, maps the signal to the frequency domain. At each DFT sample frequency $f_k = \frac{k}{n}$ for $k = 1, \dots, n - 1$, the DFT value $\mathcal{F}(\mathbf{x})[f_k]$ represents the complex-valued frequency component in the signal. We define the signal’s *power spectral density* as the expected squared magnitude (the power) of the signal at different sample frequencies

$$S(f_k) = \mathbb{E}_{\mathbf{x}} \left[\frac{|\mathcal{F}(\mathbf{x})[f_k]|^2}{n} \right]. \quad (8)$$

When $S(f_k) = c|f_k|^{-\beta}$ for constants $c, \beta > 0$, we say that the signal follows a power law in the frequency domain with parameters c, β .

3. Related Work

Inverse problems of the form in Equation (1) have been solved for many years with different priors, such as sparse/low-rank priors [4–6] or generative priors [3, 29]. In this work, we focus on posterior sampling methods that use pretrained diffusion models and approximate the conditional score to perform guidance [8, 9, 19, 30, 33, 35, 40]. These have been applied to inverse problems such as image deblurring, super-resolution [11], and image inpainting [9, 27]. However, they can incur significant approximation errors as we will illustrate in Section 4.1. Works such as [10, 41] propose methods to mitigate these approximation errors, but rely on strong assumptions on the data manifold. In this work, we use a more practical assumption that the data obeys a power law in the frequency domain [38] in order to develop a new approximation.

A line of work has explored performing diffusion in a transformed space to perform guidance for inverse problems [23, 24]. This is in fact closely related to our work

as our work is akin to performing diffusion in the Fourier domain instead, similar to [28]. Building on recent connections between diffusion models and spectral autoregression [15], our work differs from previous approaches [8, 35] by using a frequency-guided measurement schedule rather than one based on the unconditional diffusion model’s variance schedule. We refer the reader to [12] for a comprehensive survey on using diffusion models for inverse problems.

4. Analysis of Approximation Error

As illustrated in Section 2.2, the main challenge in developing unsupervised inverse problem solvers is estimating the noisy likelihood score $\nabla_{\mathbf{x}_t} \log p(\mathbf{y} | \mathbf{x}_t)$, which depends on the intractable denoising distribution $p(\mathbf{x}_0 | \mathbf{x}_t)$. It is common to substitute this denoising distribution with an approximation that depends only on the posterior mean $\boldsymbol{\mu}_{0|t} = \mathbb{E}[\mathbf{x}_0 | \mathbf{x}_t]$, which is tractable using Tweedie’s formula. However, these methods can incur a significant approximation error by using simple distributions centered around the posterior mean instead of the true distribution.

We begin by understanding precisely when this approximation gap is high. Our analysis is inspired by the empirical observation that we can construct simple image restoration tasks where several state-of-the-art diffusion-based methods struggle to recover the underlying signal. Specifically, in Figure 1, we consider two inverse problems, both of which have forward operators that are convolutions with a given kernel. The first is when the kernel is a low-pass filter, such as a Gaussian blur kernel. The second is when the kernel is a high-pass filter, such as a Dirac kernel minus a Gaussian blur kernel. As expected, prior approaches such as Diffusion Posterior Sampling [9] and variants [10, 41] perform well at Gaussian deblurring. However, when the forward operator is a high-pass filter, remarkably these approaches all fail to produce coherent outputs. This failure appears to stem from a gap between the true conditional score and its estimate, which we demonstrate theoretically in the following section.

4.1. Theoretical Analysis

Our first contribution is a precise characterization of the approximation errors in Diffusion Posterior Sampling (DPS), a popular inverse problem solver, under specific distributional assumptions. To explain the phenomenon in Figure 1, our analysis requires two key properties.

1. We need to analyze the frequency characteristics of the data as well as the interplay between the frequency characteristics of the data and the forward operator.
2. To quantify the approximation gap, we need to compute the true conditional score.

For the first property, we can look at the power spectral den-

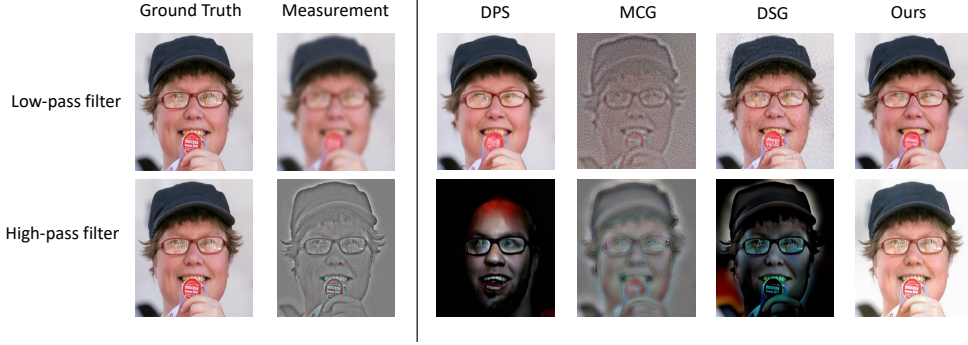


Figure 1. Even for linear inverse problems, SOTA diffusion-based methods (DPS, MCG, DSG) can struggle to solve inverse problems when the forward operator is convolution with a high-pass filter. In contrast, our method is still able to achieve a high quality reconstruction.

sity of the data, as defined in Equation (8), which tells us how much the signal’s power is distributed across different frequencies. For the second property, it is natural to consider a setting where the clean data \mathbf{x}_0 is drawn from a multivariate Gaussian distribution. Although these two properties seem to be at odds, the following lemma establishes an equivalence between the power spectral density of the data and its covariance.

Lemma 1. *Let $f_k = \frac{k}{n}$ for $k = 0, \dots, n-1$ denote the DFT sample frequencies for a signal of length n . There exists a covariance matrix Σ_f such that for $\mathbf{x} \sim \mathcal{N}(\mathbf{0}, \Sigma_f)$, the following two properties hold. First, the signal \mathbf{x} follows a power law in the frequency domain with parameters $c, \beta > 0$, i.e., it has a power spectral density $S(f_k) = c|f_k|^{-\beta}$ for the non-zero DFT sample frequencies f_k . Second, the eigenvalues of Σ_f are precisely $c|f_k|^{-\beta}$.*

This is a special case of a classical result known as the Wiener-Khinchin Theorem [7]. Note that this does not imply that all random vectors that follow a power law in the frequency domain are Gaussian. For example, natural image data tends to follow a radially averaged power law in the frequency domain, but is far from being distributed as a Gaussian [38]. Nonetheless, this lemma guides us in understanding the approximation gap in a setting that mimics the frequency characteristics of natural image data.

Next, we quantify the approximation gap under a multivariate Gaussian assumption on the data. Let $s^*(\mathbf{x}_t, \mathbf{y}) = \nabla_{\mathbf{x}_t} \log p(\mathbf{x}_t | \mathbf{y})$ be the true conditional score and let $s^{\text{DPS}}(\mathbf{x}_t, \mathbf{y})$ be the approximation of the score utilized by DPS. Recall that the main approximation used by DPS is

$$s^{\text{DPS}}(\mathbf{x}_t, \mathbf{y}) = \nabla_{\mathbf{x}_t} \log p(\mathbf{x}_t) + \nabla_{\mathbf{x}_t} \log p(\mathbf{y} | \boldsymbol{\mu}_{0|t}), \quad (9)$$

where $\boldsymbol{\mu}_{0|t} = \mathbb{E}[\mathbf{x}_0 | \mathbf{x}_t]$. Note that $\boldsymbol{\mu}_{0|t}$ is a function of \mathbf{x}_t .

Theorem 2. *Suppose \mathbf{x}_0 is drawn from $\mathcal{N}(\mathbf{0}, \Sigma)$ and we are given linear measurements $\mathbf{y} = \mathcal{A}(\mathbf{x}_0) + \mathbf{z}$, where $\mathcal{A}(\mathbf{x}_0) = \mathbf{A}\mathbf{x}_0$ and $\mathbf{z} \sim \mathcal{N}(\mathbf{0}, \sigma_y^2 \mathbf{I})$. Suppose that the intermedi-*

ate value \mathbf{x}_t of the continuous-time reverse diffusion from Equation (5) can be written as $\mathbf{x}_t = \sqrt{\bar{\alpha}_t}\mathbf{x}_0 + \sqrt{1 - \bar{\alpha}_t}\epsilon$ where $\epsilon \sim \mathcal{N}(\mathbf{0}, \mathbf{I})$. Then, we have that

$$\nabla_{\mathbf{x}_t} \log p(\mathbf{y} | \mathbf{x}_t) = (\mathbf{A}\Gamma_t)^T (\mathbf{A}\Sigma_{0|t}\mathbf{A}^T + \sigma_y^2 \mathbf{I})^{-1} \boldsymbol{\Delta}_t, \quad (10)$$

where $\Gamma_t = \sqrt{\bar{\alpha}_t}\Sigma(\bar{\alpha}_t\Sigma + (1 - \bar{\alpha}_t)\mathbf{I})^{-1}$, $\boldsymbol{\mu}_{0|t} = \mathbb{E}[\mathbf{x}_0 | \mathbf{x}_t] = \Gamma_t\mathbf{x}_t$, $\Sigma_{0|t} = \text{Cov}[\mathbf{x}_0 | \mathbf{x}_t] = \Sigma - \sqrt{\bar{\alpha}_t}\Gamma_t\Sigma$, and $\boldsymbol{\Delta}_t = \mathbf{y} - \mathbf{A}\boldsymbol{\mu}_{0|t}$. Moreover, the approximation gap $\mathcal{J}^{\text{DPS}} := s^{\text{DPS}}(\mathbf{x}_t, \mathbf{y}) - s^(\mathbf{x}_t, \mathbf{y})$ is given by:*

$$\mathcal{J}^{\text{DPS}} = (\mathbf{A}\Gamma_t)^T (\sigma_y^{-2}\mathbf{I} - (\mathbf{A}\Sigma_{0|t}\mathbf{A}^T + \sigma_y^2 \mathbf{I})^{-1}) \boldsymbol{\Delta}_t. \quad (11)$$

The proof is in Appendix B. The $\bar{\alpha}_t$ corresponds to the variance schedule of standard diffusion models such as DDPM [20]. Our assumption that $\mathbf{x}_t = \sqrt{\bar{\alpha}_t}\mathbf{x}_0 + \sqrt{1 - \bar{\alpha}_t}\epsilon$ isolates the effects of the approximation gap as the generated sample is exactly \mathbf{x}_0 . While we characterize this approximation gap only for DPS, this framework allows us to analytically study the gaps of many other methods, such as Π -GDM [33], since we have a formula for the noisy likelihood score. A detailed study of other works and their approximation errors would be a useful area of future work.

4.2. Empirical Study

Armed with Lemma 1 and Theorem 2, we now study the approximation gap and how the forward operator \mathcal{A} interacts with Σ depending on how it affects certain frequency ranges. To do this, we first generate 1-D signals $\mathbf{x}_0 \sim \mathcal{N}(\mathbf{0}, \Sigma_f)$ that follow a power law in the frequency domain using the construction of Σ_f given in Lemma 1. The corresponding measurements for these signals are $\mathbf{y} = \mathbf{A}\mathbf{x}_0 + \mathbf{z}$ with $\mathbf{z} \sim \mathcal{N}(\mathbf{0}, \mathbf{I})$. As in Figure 1, we let \mathcal{A} be a low-pass filter or a high-pass filter, where the low-pass filter is a Gaussian kernel of standard deviation σ , denoted as $g(\sigma)$, and the high pass filter is a Dirac kernel minus $g(\sigma)$. We then calculate the exact approximation gap between DPS and the true conditional score using Theorem 2 for different

diffusion timesteps. The full experimental details of this study can be found in Appendix D.

Figure 2 shows the DPS approximation gap as a function of the diffusion timesteps (where higher timesteps correspond to a lower value of $\bar{\alpha}_t$) for the variance schedule used in the DDPM model for $T = 1000$ [20]. We clearly see two different trends depending on the forward operator. When the operator is a low-pass filter, the DPS approximation gap is low when t is either close to T or close to 1. When the operator is a high-pass filter, the DPS approximation worsens significantly as we increase t , likely because noise affecting higher frequency ranges in \mathbf{x}_t is amplified by the high-pass filter. In the initial stages of the reverse process, the estimated conditional score is very inaccurate, corroborating the issues seen in Figure 1. To the best of our knowledge, this is the first time any distributional assumptions have been used to characterize the exact gap between the DPS approximation and the true conditional score. While [9] and [41] provide upper and lower bounds on this gap, known as the Jensen gap, these bounds do not exploit the structure of the data distribution and as such, can be loose.

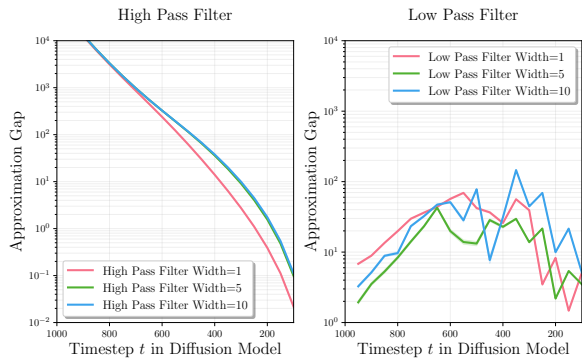


Figure 2. We show the exact approximation gap for DPS across diffusion timesteps when the data follows a power law in the frequency domain and the forward operator is a low-pass filter or a high-pass filter of varying widths. The width denotes the σ of the Gaussian kernel. Note the y -axis is in log-scale.

5. Frequency Guided Posterior Sampling

While the results from Figures 1 and 2 might appear artificial, this phenomenon frequently emerges in complex real-world image restoration problems. For example, in directional motion deblurring, the forward operator does indeed act as a high-pass filter in certain spatial directions of the image (see Appendix C). Unfortunately, for real image data that follows a complex non-Gaussian distribution, we cannot exactly compute the true conditional score as we did in Theorem 2. Despite this, we hope to derive practical insights from our theoretical analysis because the underlying data distribution in our synthetic experiments mimics the

frequency distribution of natural images.

Specifically, Figure 2 reveals a crucial insight: when using a low-pass filter as the forward operator, the approximation gap remains small during the early stages of the reverse process. Diffusion models inherently generate images hierarchically, from coarse to fine details, so the early stages of the reverse process play a crucial role in establishing the fundamental structure that matches the measurements. If the approximation gap is large in this regime, as is the case when the forward operator is a high-pass filter, it is unlikely the sampling procedure will produce a good reconstruction.

We propose a simple fix to this issue by constraining the measurements to retain only low frequency components at the initial steps of the reverse process and progressively add in high frequency components. This intuitively aligns the frequency characteristics of the measurements with the iterates of the diffusion reverse process. To implement this, we convolve the original measurement \mathbf{y} with a time-varying low-pass filter \mathbf{k}_t . Denoting $\phi_t(\mathbf{y})$ as this convolution, the approximation we propose for the noisy likelihood score is

$$\nabla_{\mathbf{x}_t} \log p(\mathbf{y} | \mathbf{x}_t) \approx \nabla_{\mathbf{x}_t} \log p(\phi_t(\mathbf{y}) | \boldsymbol{\mu}_{0|t}), \quad (12)$$

where $\boldsymbol{\mu}_{0|t}$ denotes the Tweedie estimate $\mathbb{E}[\mathbf{x}_0 | \mathbf{x}_t]$ predicted by the diffusion model. In order to compute the above approximation, we need to compute the model likelihood for the new measurements. Since convolution of a signal \mathbf{y} with a low pass filter can be represented as a circulant matrix multiplied by \mathbf{y} , we have that $\phi_t(\mathbf{y}) = \mathbf{C}_t \mathbf{y}$ where \mathbf{C}_t is a time-dependent circulant matrix representing \mathbf{k}_t . Thus, using properties of the multivariate normal distribution, we have that the updated model likelihood is

$$p(\phi_t(\mathbf{y}) | \mathbf{x}_0) = \mathcal{N}(\mathbf{C}_t \mathcal{A}(\mathbf{x}_0), \sigma_y^2 \mathbf{C}_t \mathbf{C}_t^T). \quad (13)$$

Given this likelihood, our approximation of the noisy likelihood score becomes

$$p(\phi_t(\mathbf{y}) | \boldsymbol{\mu}_{0|t}) = \mathcal{N}(\mathbf{C}_t \mathcal{A}(\boldsymbol{\mu}_{0|t}), \sigma_y^2 \mathbf{C}_t \mathbf{C}_t^T), \quad (14)$$

and its corresponding gradient is

$$\nabla_{\mathbf{x}_t} \log p(\phi_t(\mathbf{y}) | \boldsymbol{\mu}_{0|t}) = \mathbf{S}_t \nabla_{\mathbf{x}_t} \left\| \mathbf{C}_t \mathbf{y} - \mathbf{C}_t \mathcal{A}(\boldsymbol{\mu}_{0|t}) \right\|_2^2, \quad (15)$$

where $\mathbf{S}_t = (\sigma_y^2 \mathbf{C}_t \mathbf{C}_t^T)^{-1}$. Since $\boldsymbol{\mu}_{0|t}$ can be computed using one network evaluation of the diffusion model, its gradient with respect to \mathbf{x}_t can be computed via backpropagation, as in DPS. Alternating unconditional sampling and conditional sampling using their corresponding score functions gives us our algorithm, which we call **Frequency Guided Posterior Sampling (FGPS)** outlined in Algorithm 1.

Dataset-informed choice of \mathbf{k}_t . An important choice for our method is choosing the sequence $\{\mathbf{k}_t\}_{t=1}^T$. Each \mathbf{k}_t is a

low-pass filter that should allow frequencies up till a threshold τ_t and then strongly attenuate any frequencies above τ_t . In order to encode that the initial steps of the reverse process should only use low frequency components of \mathbf{y} , we require that τ_T should start off small and increase as t decreases. We denote the sequence of τ_t as our frequency curriculum. As datasets can have varying frequency characteristics, we set our frequency curriculum in a data-dependent way, as explained in Section 6.

Implementation Details. We efficiently compute $\phi_t(\cdot)$ in the Fourier domain. Specifically, \mathbf{C}_t can be diagonalized as $\mathbf{C}_t = \mathbf{F}^{-1}\mathbf{M}\mathbf{F}$, where \mathbf{F} denotes the Discrete Fourier Transform matrix [37]. Using this property along with the fact that \mathbf{F} is an orthogonal matrix, we have that $p(\phi_t(\mathbf{y}) \mid \boldsymbol{\mu}_{0|t}) = p(\mathbf{F}\phi_t(\mathbf{y}) \mid \boldsymbol{\mu}_{0|t}) = p(\mathbf{M}\mathbf{F}\mathbf{y} \mid \boldsymbol{\mu}_{0|t})$. Thus, we compute $\phi_t(\mathbf{y})$ and $\phi_t(\mathcal{A}(\boldsymbol{\mu}_{0|t}))$ by first taking the Fast Fourier Transform of the input and applying a mask in the frequency domain, which adds minimal computational overhead (see Appendix D). For simplicity, the mask for filter $\phi_t(\cdot)$ is a binary mask that zeroes out the frequency components larger than τ_t .

Algorithm 1 Frequency Guided Posterior Sampling

Require: $\mathbf{y}, \mathcal{A}, \{\phi_t(\cdot), \mathbf{S}_t, \alpha_t, \tilde{\sigma}_t\}_{t=1}^T$

- 1: $\mathbf{x}_T \sim \mathcal{N}(\mathbf{0}, \mathbf{I})$
- 2: **for** $t \leftarrow T$ to 1 **do**
- 3: $\hat{\mathbf{s}} \leftarrow s_\theta(\mathbf{x}_t, t)$
- 4: $\bar{\alpha}_t \leftarrow \prod_{j=1}^t \alpha_j$
- 5: $\boldsymbol{\mu}_{0|t} \leftarrow \frac{1}{\sqrt{\bar{\alpha}_t}}(\mathbf{x}_t + (1 - \bar{\alpha}_t)\hat{\mathbf{s}})$
- 6: $\mathbf{z} \sim \mathcal{N}(\mathbf{0}, \mathbf{I})$
- 7: $\mathbf{x}'_{t-1} \leftarrow \frac{\sqrt{\alpha_t(1-\bar{\alpha}_{t-1})}}{1-\bar{\alpha}_t}\mathbf{x}_t + \frac{\sqrt{\bar{\alpha}_{t-1}(1-\alpha_t)}}{1-\bar{\alpha}_t}\boldsymbol{\mu}_{0|t} + \tilde{\sigma}_t\mathbf{z}$
- 8: $\mathbf{x}_{t-1} \leftarrow \mathbf{x}'_{t-1} - \mathbf{S}_t \nabla_{\mathbf{x}_t} \|\phi_t(\mathbf{y}) - \phi_t(\mathcal{A}(\boldsymbol{\mu}_{0|t}))\|_2^2$
- 9: **end for**

6. Experiments

To empirically validate the performance of FGPS, we begin by investigating the approximation gap of our method on synthetic data as in Figure 2. Then, we evaluate our method on several real-world datasets and image restoration tasks, where we demonstrate compelling performance of our method as compared to state-of-the-art baselines.

6.1. Synthetic Data: FGPS Approximation Gap

From Theorem 2, we know that under a multivariate normal assumption on the data, the posterior mean $\boldsymbol{\mu}_{0|t}$ is $\boldsymbol{\Gamma}_t \mathbf{x}_t$. Under the same assumptions as Theorem 2, for linear inverse problems where $\mathcal{A}(\mathbf{x}_0) = \mathbf{A}\mathbf{x}_0$ we analytically compute our approximation to the noisy likelihood score given in Equation (15) as

$$(\mathbf{C}_t \mathbf{A})^T (\sigma_y^2 \mathbf{C}_t \mathbf{C}_t^T)^{-1} (\mathbf{C}_t \mathbf{y} - \mathbf{C}_t \mathbf{A} \boldsymbol{\mu}_{0|t}). \quad (16)$$

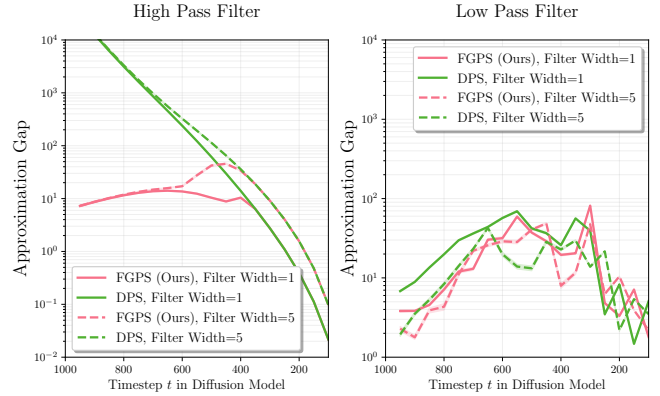


Figure 3. We use the same setup as Figure 2. Our method has a significantly smaller approximation gap than DPS when the forward operator is a high-pass filter. Note the y -axis is in log-scale.

Theorem 2 gives an exact expression for the true noisy likelihood score, so the approximation gap of our method can also be computed analytically. In Figure 3, we plot the approximation gap of our method (with frequency curriculum given in Appendix D) as compared to DPS. We find that in the early steps of the reverse process, our method has an approximation gap that is several orders of magnitude smaller than DPS when the forward operator is a high-pass filter. As the early stages of the reverse process are when the generated image develops coarse features, we argue it is crucial that the approximation gap is small in these phases.

6.2. Real-World Data

Datasets. We evaluate our method on two datasets: the Flickr-Faces-HQ (FFHQ 256x256) dataset of high-resolution faces [22], and the ImageNet-1000 dataset of diverse objects [13]. We utilize pretrained diffusion models from [9] and [14] for the FFHQ and ImageNet datasets respectively, using a class-conditional model for ImageNet.

Tasks. We consider four challenging image restoration tasks for our experimental evaluation. The first three are linear inverse problems: Gaussian deblurring, motion deblurring, and deconvolution with a high-pass filter. The last is a nonlinear inverse problem: image dehazing. The details of the four forward operators we consider can be found in Appendix D. All measurements have Gaussian measurement noise added with standard deviation 0.05.

Baselines and Metrics. We compare against several competitive unsupervised methods. The first two baselines are popular unsupervised diffusion-based solvers: Diffusion Posterior Sampling (DPS) [9], a method that approximates the conditional score with a Dirac delta around the posterior mean, and Score-SDE/ILVR [8, 35], a method that uses a sequence of noisy measurements computed using the

Method	Gaussian Blur				Motion Blur				High-Pass Filter			
	FID↓	LPIPS↓	PSNR↑	SSIM↑	FID↓	LPIPS↓	PSNR↑	SSIM↑	FID↓	LPIPS↓	PSNR↑	SSIM↑
FFHQ Dataset												
Score-SDE/ILVR [8, 35]	58.79	0.266	23.34	0.648	69.10	0.387	18.59	0.457	85.35	0.356	11.86	0.600
MCG [10]	310.33	1.035	11.64	0.143	296.93	0.771	11.54	0.127	151.77	0.581	<u>12.48</u>	0.466
DPS [9]	21.69	0.116	26.01	0.743	<u>27.15</u>	<u>0.153</u>	24.17	<u>0.688</u>	121.57	0.694	6.17	0.222
DSG [41]	44.63	0.294	22.75	0.633	32.74	0.257	25.66	0.687	<u>17.81</u>	0.246	12.12	<u>0.695</u>
FGPS (Ours)	<u>21.89</u>	<u>0.139</u>	<u>25.44</u>	<u>0.727</u>	20.48	0.127	<u>25.48</u>	0.723	10.02	0.124	18.79	0.739
ImageNet Dataset												
Score-SDE/ILVR [8, 35]	104.81	0.676	16.27	0.318	100.54	0.665	16.62	0.290	226.51	0.784	10.69	0.345
MCG [10]	320.63	1.005	12.01	0.121	306.43	0.963	11.80	0.076	295.10	1.000	<u>11.62</u>	0.278
DPS [9]	98.02	0.517	17.35	0.364	<u>77.74</u>	<u>0.407</u>	<u>20.90</u>	<u>0.551</u>	111.73	0.569	10.66	<u>0.396</u>
DSG [41]	87.51	0.375	<u>20.75</u>	<u>0.524</u>	107.25	0.453	19.58	0.488	<u>110.85</u>	0.546	8.425	0.382
FGPS (Ours)	56.46	0.294	21.70	0.574	49.25	0.267	22.01	0.601	24.44	0.192	15.96	0.686

Table 1. Quantitative comparison of different methods on 1000 images from the FFHQ and Imagenet validation datasets. Bolded entries indicate best performance and underlined entries indicate second best performance.



Figure 4. Qualitative results on FFHQ and ImageNet datasets. The dotted red boxes highlight areas of the image where our method results in higher-quality reconstructions than DPS and DSG. Zoomed in versions can be found in the Appendix.

diffusion model variance schedule. Then, we compare to two state-of-the-art methods focused on mitigating the approximation gap problem: Manifold Constrained Gradient (MCG) [10], which after each denoising timestep performs a projection onto an estimate of the noisy data manifold, and Diffusion with Spherical Guidance (DSG) [41], which restricts the guidance step using a spherical Gaussian constraint. For image dehazing, we further compare to two problem-specific baselines: DoubleDIP [18], an unsupervised method which uses a dark channel prior to estimate

the dehazed image, and AOD-Net [26], a supervised method trained to dehaze images from pairs of clean-hazy images. For fairness, we use the same pretrained score function for all diffusion-based methods. We evaluate our method on two perceptual metrics, FID and LPIPS distance, and two distortion-based metrics, PSNR and SSIM.

Frequency Curriculum. For both FFHQ and ImageNet across all tasks, in our method we set τ_1 and τ_T to be $\frac{75 \cdot 100}{256} \%$ and $\frac{10 \cdot 100}{256} \%$ of the overall frequency range respectively. We set different frequency curricula for the two

datasets as described in Section 5. Specifically, our experiments (shown in Appendix F) reveal that on deblurring tasks on FFHQ, our method performs better with an exponentially increasing schedule between τ_T and τ_1 , while on ImageNet, our method achieves better results with a linear schedule.

Step Size Schedule. Similar to DPS, we replace the theoretical quantity \mathbf{S}_t for the conditional sampling step with $\frac{\kappa}{\|\phi_t(y) - \phi(\mathcal{A}(\mu_{0|t}))\|_2} \mathbf{I}$ for a hyperparameter κ , which works well in practice. Using the intuition from Figure 3 that the approximation gap is small in the initial steps of the reverse process, we set κ large initially and decay it following a cosine curve.

Results on Linear Inverse Problems. Table 1 shows our main results for linear inverse problems. On the Gaussian blurring task, surprisingly even though the forward operator already acts as a low-pass filter, our method significantly improves upon DPS and DSG on the Imagenet dataset. This indicates the benefit of the frequency curriculum on more complex and diverse datasets, a phenomenon also demonstrated qualitatively in Figure 4. On the more complex image restoration tasks, our method outperforms the baselines in almost all metrics. Notably, even though ScoreSDE/ILVR uses a sequence of noisy measurements, this sequence is not adapted to the frequency characteristics of the data, which results in lower-quality reconstructions as compared to our method (see Appendix E for further discussion). In Figure 4, we see the qualitative differences between the methods. For high-pass filter operators, existing methods generate visually implausible images, indicating that the approximation errors push the denoised outputs away from the natural image manifold. In contrast, our method is able to accurately reconstruct the underlying ground truth image. For blurry images, we see that DPS tends to produce smoothed images, losing high-frequency details. While DSG is able to improve upon this and generate images with fine-grained characteristics of the underlying image, it tends to also generate artifacts. In contrast, due to our frequency curriculum, our method is able to generate images with high perceptual quality. We give further qualitative comparisons to all baselines in Appendix F.

Results on Image Dehazing. Table 2 shows our main results for the nonlinear image dehazing task on the FFHQ dataset. A key strength of our method is the ability to handle nonlinear inverse problems, unlike methods such as [8, 24, 35]. In Figure 4, we observe that our method successfully reconstructs finer details such as background details and facial characteristics similar to what we observed for linear inverse problems. DSG produces slightly grainy reconstructions, but performs much better on the dehazing task than the other tasks. Due to the powerful generative capacity of diffusion models, our method also performs bet-

ter than problem-specific supervised methods such as AOD-Net [26], a phenomenon also observed in [33]. We provide more qualitative examples in Appendix F.

Method	FID↓	LPIPS↓	PSNR↑	SSIM↑
DoubleDIP [18]	50.51	0.500	13.80	0.483
AOD-Net [26]	33.35	0.325	17.42	0.532
DPS [9]	24.24	0.137	25.88	0.806
DSG [41]	<u>10.55</u>	<u>0.134</u>	<u>26.07</u>	<u>0.795</u>
FGPS (Ours)	9.37	0.066	26.88	0.840

Table 2. Comparison of different haze removal methods. Bolded entries indicate best performance and underlined entries indicate second best performance.

Effect of Frequency Curriculum. A key ingredient of our method is the frequency curriculum with a time-varying low pass filter \mathbf{k}_t . To understand the effect of this curriculum, we compare taking a time-dependent \mathbf{k}_t vs. a fixed \mathbf{k} that zeroes out frequencies above τ_1 for all t . In Figure 5, we see that for the high-pass filter operator, the generated reconstructions are still visually implausible images for a fixed \mathbf{k} , indicating the frequency curriculum is crucial to our method. We examine this in detail in Appendix F as well as conduct further ablation studies.

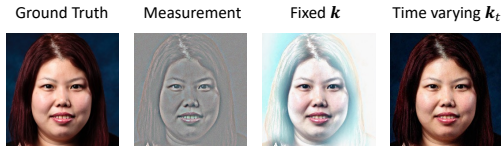


Figure 5. Qualitative Ablation Study: fixed low-pass filter vs. time-dependent low pass filter.

7. Conclusion

In this paper, we provide a theoretical analysis characterizing the approximation error in existing diffusion-based restoration methods, demonstrating how these errors can become severe when forward operators interact with high-frequency components of images. Then, motivated by these insights, we introduce Frequency Guided Posterior Sampling (FGPS), a method that progressively incorporates frequency information during the restoration process in a data-dependent manner. Our extensive experiments on challenging image restoration tasks, such as motion deblurring and image dehazing, demonstrate that FGPS significantly outperforms existing methods. This work opens up new directions for analyzing and improving diffusion model performance on inverse problems by carefully considering the frequency characteristics of both the data and the degradation process.

References

- [1] Brian DO Anderson. Reverse-time diffusion equation models. *Stochastic Processes and their Applications*, 12(3):313–326, 1982. 2
- [2] Christopher M Bishop and Nasser M Nasrabadi. *Pattern recognition and machine learning*. Springer, 2006. 2
- [3] Ashish Bora, Ajil Jalal, Eric Price, and Alexandros G Dimakis. Compressed sensing using generative models. In *International conference on machine learning*, pages 537–546. PMLR, 2017. 1, 3
- [4] Emmanuel Candes and Benjamin Recht. Exact matrix completion via convex optimization. *Communications of the ACM*, 55(6):111–119, 2012. 1, 3
- [5] Emmanuel J Candes, Justin K Romberg, and Terence Tao. Stable signal recovery from incomplete and inaccurate measurements. *Communications on Pure and Applied Mathematics: A Journal Issued by the Courant Institute of Mathematical Sciences*, 59(8):1207–1223, 2006. 1
- [6] Emmanuel J Candès, Xiaodong Li, Yi Ma, and John Wright. Robust principal component analysis? *Journal of the ACM (JACM)*, 58(3):1–37, 2011. 1, 3
- [7] David C Champeney. *A handbook of Fourier theorems*, chapter 11. Cambridge University Press, 1987. 4
- [8] Jooyoung Choi, Sungwon Kim, Yonghyun Jeong, Youngjune Gwon, and Sungroh Yoon. Ilvr: Conditioning method for denoising diffusion probabilistic models. *arXiv preprint arXiv:2108.02938*, 2021. 3, 6, 7, 8, 4
- [9] Hyungjin Chung, Jeongsol Kim, Michael T Mccann, Marc L Klasky, and Jong Chul Ye. Diffusion posterior sampling for general noisy inverse problems. *arXiv preprint arXiv:2209.14687*, 2022. 1, 3, 5, 6, 7, 8, 4
- [10] Hyungjin Chung, Byeongsu Sim, Dohoon Ryu, and Jong Chul Ye. Improving diffusion models for inverse problems using manifold constraints. *Advances in Neural Information Processing Systems*, 35:25683–25696, 2022. 2, 3, 7, 4
- [11] Max Daniels, Tyler Maunu, and Paul Hand. Score-based generative neural networks for large-scale optimal transport. *Advances in neural information processing systems*, 34:12955–12965, 2021. 3
- [12] Giannis Daras, Hyungjin Chung, Chieh-Hsin Lai, Yuki Mitsufuji, Jong Chul Ye, Peyman Milanfar, Alexandros G Dimakis, and Mauricio Delbracio. A survey on diffusion models for inverse problems. *arXiv preprint arXiv:2410.00083*, 2024. 3, 4
- [13] Jia Deng, Wei Dong, Richard Socher, Li-Jia Li, Kai Li, and Li Fei-Fei. Imagenet: A large-scale hierarchical image database. In *2009 IEEE conference on computer vision and pattern recognition*, pages 248–255. Ieee, 2009. 6
- [14] Prafulla Dhariwal and Alexander Nichol. Diffusion models beat gans on image synthesis. *Advances in neural information processing systems*, 34:8780–8794, 2021. 1, 6
- [15] Sander Dieleman. Diffusion is spectral autoregression, 2024. 3
- [16] David L Donoho, Michael Elad, and Vladimir N Temlyakov. Stable recovery of sparse overcomplete representations in the presence of noise. *IEEE Transactions on information theory*, 52(1):6–18, 2005. 1
- [17] Bradley Efron. Tweedie’s formula and selection bias. *Journal of the American Statistical Association*, 106(496):1602–1614, 2011. 2, 3, 1
- [18] Yosef Gandelsman, Assaf Shocher, and Michal Irani. "double-dip": unsupervised image decomposition via coupled deep-image-priors. In *Proceedings of the IEEE/CVF conference on computer vision and pattern recognition*, pages 11026–11035, 2019. 7, 8
- [19] Jonathan Ho and Tim Salimans. Classifier-free diffusion guidance. *arXiv preprint arXiv:2207.12598*, 2022. 3
- [20] Jonathan Ho, Ajay Jain, and Pieter Abbeel. Denoising diffusion probabilistic models. *Advances in neural information processing systems*, 33:6840–6851, 2020. 1, 2, 4, 5
- [21] Jonathan Ho, Tim Salimans, Alexey Gritsenko, William Chan, Mohammad Norouzi, and David J Fleet. Video diffusion models. *Advances in Neural Information Processing Systems*, 35:8633–8646, 2022. 1
- [22] Tero Karras, S. Laine, and Timo Aila. A style-based generator architecture for generative adversarial networks. *2019 IEEE/CVF Conference on Computer Vision and Pattern Recognition (CVPR)*, pages 4396–4405, 2019. 6
- [23] Bahjat Kawar, Gregory Vaksman, and Michael Elad. Snips: Solving noisy inverse problems stochastically. *Advances in Neural Information Processing Systems*, 34:21757–21769, 2021. 3
- [24] Bahjat Kawar, Michael Elad, Stefano Ermon, and Jiaming Song. Denoising diffusion restoration models. *Advances in Neural Information Processing Systems*, 35:23593–23606, 2022. 1, 3, 8, 5
- [25] Zhifeng Kong, Wei Ping, Jiayi Huang, Kexin Zhao, and Bryan Catanzaro. Diffwave: A versatile diffusion model for audio synthesis. *arXiv preprint arXiv:2009.09761*, 2020. 1
- [26] Boyi Li, Xiulian Peng, Zhangyang Wang, Jizheng Xu, and Dan Feng. Aod-net: All-in-one dehazing network. In *Proceedings of the IEEE international conference on computer vision*, pages 4770–4778, 2017. 7, 8
- [27] Andreas Lugmayr, Martin Danelljan, Andres Romero, Fisher Yu, Radu Timofte, and Luc Van Gool. Repaint: Inpainting using denoising diffusion probabilistic models. In *Proceedings of the IEEE/CVF conference on computer vision and pattern recognition*, pages 11461–11471, 2022. 3
- [28] Xiaoqian Lv, Shengping Zhang, Chenyang Wang, Yichen Zheng, Bineng Zhong, Chongyi Li, and Liqiang Nie. Fourier priors-guided diffusion for zero-shot joint low-light enhancement and deblurring. In *Proceedings of the IEEE/CVF Conference on Computer Vision and Pattern Recognition*, pages 25378–25388, 2024. 3
- [29] Xingang Pan, Xiaohang Zhan, Bo Dai, Dahua Lin, Chen Change Loy, and Ping Luo. Exploiting deep generative prior for versatile image restoration and manipulation. *IEEE Transactions on Pattern Analysis and Machine Intelligence*, 44(11):7474–7489, 2021. 1, 3
- [30] François Rozet, G r me Andry, Fran ois Lanusse, and Gilles Louppe. Learning diffusion priors from observations by expectation maximization. *arXiv preprint arXiv:2405.13712*, 2024. 3

- [31] Leonid I Rudin, Stanley Osher, and Emad Fatemi. Nonlinear total variation based noise removal algorithms. *Physica D: nonlinear phenomena*, 60(1-4):259–268, 1992. [1](#)
- [32] Chitwan Saharia, William Chan, Huiwen Chang, Chris Lee, Jonathan Ho, Tim Salimans, David Fleet, and Mohammad Norouzi. Palette: Image-to-image diffusion models. In *ACM SIGGRAPH 2022 conference proceedings*, pages 1–10, 2022. [1](#), [2](#)
- [33] Jiaming Song, Arash Vahdat, Morteza Mardani, and Jan Kautz. Pseudoinverse-guided diffusion models for inverse problems. In *International Conference on Learning Representations*, 2023. [1](#), [3](#), [4](#), [8](#)
- [34] Yang Song and Stefano Ermon. Generative modeling by estimating gradients of the data distribution. *Advances in neural information processing systems*, 32, 2019. [1](#), [2](#)
- [35] Yang Song, Jascha Sohl-Dickstein, Diederik P Kingma, Abhishek Kumar, Stefano Ermon, and Ben Poole. Score-based generative modeling through stochastic differential equations. *arXiv preprint arXiv:2011.13456*, 2020. [1](#), [2](#), [3](#), [6](#), [7](#), [8](#), [4](#)
- [36] Andrew M Stuart. Inverse problems: a bayesian perspective. *Acta numerica*, 19:451–559, 2010. [1](#)
- [37] Marco Alexander Treiber. *Optimization for computer vision*. Springer, 2013. [6](#)
- [38] van A Van der Schaaf and JH van van Hateren. Modelling the power spectra of natural images: statistics and information. *Vision research*, 36(17):2759–2770, 1996. [3](#), [4](#), [5](#)
- [39] Pascal Vincent. A connection between score matching and denoising autoencoders. *Neural computation*, 23(7):1661–1674, 2011. [2](#)
- [40] Yinhuai Wang, Jiwen Yu, and Jian Zhang. Zero-shot image restoration using denoising diffusion null-space model. *arXiv preprint arXiv:2212.00490*, 2022. [1](#), [3](#)
- [41] Lingxiao Yang, Shutong Ding, Yifan Cai, Jingyi Yu, Jingya Wang, and Ye Shi. Guidance with spherical gaussian constraint for conditional diffusion. *arXiv preprint arXiv:2402.03201*, 2024. [2](#), [3](#), [5](#), [7](#), [8](#), [4](#)

Frequency-Guided Posterior Sampling for Diffusion-Based Image Restoration

Supplementary Material

A. Further Background

A.1. Diffusion Models

Recall that unconditional diffusion models learn the score function $\nabla_{\mathbf{x}_t} \log p(\mathbf{x})$ through denoising score matching. Assuming we have learned a neural network that approximates this score well, the backbone of most state of the art diffusion-based inverse problem solvers is the estimation of $\mu_{0|t} = \mathbb{E}[\mathbf{x}_0 | \mathbf{x}_t]$ using the learned diffusion model. This is known as Tweedie’s formula, which we state below.

Lemma 3. (Tweedie’s formula [17]) Suppose $p(\mathbf{x}_t | \mathbf{x}_0) = \mathcal{N}(\sqrt{\alpha_t}\mathbf{x}_0, (1 - \alpha_t)\mathbf{I})$. Then the posterior mean is

$$\mathbb{E}[\mathbf{x}_0 | \mathbf{x}_t] = \frac{1}{\sqrt{\alpha_t}}(\mathbf{x}_t + (1 - \alpha_t)\nabla_{\mathbf{x}_t} \log p(\mathbf{x}_t)) \quad (17)$$

Proof. We expand the score function as

$$\nabla_{\mathbf{x}_t} \log p(\mathbf{x}_t) = \frac{\nabla_{\mathbf{x}_t} p(\mathbf{x}_t)}{p(\mathbf{x}_t)} \quad (18)$$

$$= \frac{1}{p(\mathbf{x}_t)} \int \nabla_{\mathbf{x}_t} p(\mathbf{x}_t | \mathbf{x}_0) p(\mathbf{x}_0) d\mathbf{x}_0. \quad (19)$$

We can rewrite $\nabla_{\mathbf{x}_t} p(\mathbf{x}_t | \mathbf{x}_0)$ as $p(\mathbf{x}_t | \mathbf{x}_0) \nabla_{\mathbf{x}_t} \log p(\mathbf{x}_t | \mathbf{x}_0)$ and group $\frac{p(\mathbf{x}_t | \mathbf{x}_0) p(\mathbf{x}_0)}{p(\mathbf{x}_t)} = p(\mathbf{x}_0 | \mathbf{x}_t)$ to give

$$= \int p(\mathbf{x}_0 | \mathbf{x}_t) \nabla_{\mathbf{x}_t} \log p(\mathbf{x}_t | \mathbf{x}_0) d\mathbf{x}_0 \quad (20)$$

$$= \int p(\mathbf{x}_0 | \mathbf{x}_t) \frac{\sqrt{\alpha_t}\mathbf{x}_0 - \mathbf{x}_t}{1 - \alpha_t} d\mathbf{x}_0 \quad (21)$$

$$= \frac{\sqrt{\alpha_t} \mathbb{E}[\mathbf{x}_0 | \mathbf{x}_t] - \mathbf{x}_t}{1 - \alpha_t}. \quad (22)$$

Rearranging, we have our final result that gives the posterior mean as a function of the unconditional score function. \square

A.2. Signal Processing

The Fourier transform is a fundamental tool in signal processing that decomposes a signal into its constituent frequencies. For a continuous signal $\mathbf{x}(t)$, the Fourier transform is given by

$$\mathcal{F}_{\text{cont}}(\mathbf{x})[f] = \int_{-\infty}^{\infty} \mathbf{x}(t) e^{-2\pi i f t} dt, \quad (23)$$

where i denotes the complex root of unity. In discrete domains, such as digital images, we work with the Discrete Fourier Transform (DFT). For a signal $\mathbf{x} \in \mathbb{R}^n$, we denote

its DFT as $\mathcal{F}(\mathbf{x})$, where $\mathcal{F}(\mathbf{x})[f_k]$ represents the frequency component at the k -th frequency

$$\mathcal{F}(\mathbf{x})[f_k] = \sum_{n=0}^{N-1} \mathbf{x}[n] e^{-2\pi i k n / N}. \quad (24)$$

The DFT can be expressed as a matrix operation $\mathbf{F} \in \mathbb{C}^{n \times n}$ where

$$\mathbf{F}_{jk} = \frac{1}{\sqrt{n}} e^{-2\pi i j k / n}. \quad (25)$$

This matrix \mathbf{F} is unitary. A discrete convolution operation $\mathbf{x} \otimes \mathbf{h}$ can be represented as a matrix multiplication $\mathbf{C}_h \mathbf{x}$, where \mathbf{C}_h is a circulant matrix constructed from the filter \mathbf{h} . A circulant matrix has the special property that each row is a cyclic shift of the previous row:

$$\mathbf{C}_h = \begin{bmatrix} h_0 & h_{n-1} & \cdots & h_1 \\ h_1 & h_0 & \cdots & h_2 \\ \vdots & \vdots & \ddots & \vdots \\ h_{n-1} & h_{n-2} & \cdots & h_0 \end{bmatrix}. \quad (26)$$

A fundamental property of circulant matrices is that they can be diagonalized by the DFT matrix

$$\mathbf{C}_h = \mathbf{F}^* \text{diag}(\mathcal{F}(\mathbf{h})) \mathbf{F}. \quad (27)$$

This relationship explains why convolution in the spatial domain equals pointwise multiplication in the frequency domain

$$\mathcal{F}(\mathbf{x} \otimes \mathbf{h}) = \mathcal{F}(\mathbf{x}) \odot \mathcal{F}(\mathbf{h}). \quad (28)$$

Natural images typically exhibit a power law relationship in their frequency spectrum such that

$$|\mathcal{F}(\mathbf{x})[f_k]|^2 \propto \frac{1}{|f_k|^\alpha}, \quad (29)$$

where α is typically around 2. This relationship, often called the $1/f^2$ law, arises from the fundamental structure of natural scenes:

- Natural images tend to be locally smooth with occasional sharp transitions (edges)
- Objects in natural scenes exhibit self-similarity across scales
- Natural scenes contain hierarchical structures from fine to coarse details

This power law relationship provides a strong prior for image processing tasks, as it captures the statistical regularities present in natural images. The decay of frequency components according to this law explains why natural images are compressible and why high-frequency noise is particularly noticeable in image data.

B. Proofs for Section 4.1

We first prove Lemma 1, restated below.

Lemma 4. *Let $f_k = \frac{k}{n}$ for $k = 0, \dots, n-1$ denote the DFT sample frequencies for a signal of length n . There exists a covariance matrix Σ such that for $x \sim \mathcal{N}(\mathbf{0}, \Sigma)$, the following two properties hold. First, the signal \mathbf{x} follows a power law in the frequency domain with parameters $c, \beta > 0$ i.e. it has a power spectral density $S(f_k) = c|f_k|^{-\beta}$ for the non-zero DFT sample frequencies f_k . Second, the eigenvalues of Σ are precisely $c|f_k|^{-\beta}$.*

Proof. We will first provide a construction for Σ . Let \mathbf{R} be a n -length signal that is the inverse Discrete Fourier Transform of $S(f_k) = c|f_k|^{-\beta}$ for the non-zero DFT sample frequencies f_k . We construct Σ as a circulant matrix whose first row (and column) is \mathbf{R} .

Next, we show the two properties of Σ needed to prove the lemma. First, let $\mathbf{x} \sim \mathcal{N}(\mathbf{0}, \Sigma)$. Then, \mathbf{x} can be viewed as a finite stochastic process that is zero-mean, wide-sense, and stationary. It is zero-mean trivially because \mathbf{x} is sampled from a zero-mean distribution. It is wide-sense stationary because Σ is circulant. Thus, the autocovariance function, which is exactly \mathbf{R} , depends only on the gap between two elements in the signal. From the discrete-time Wiener-Khinchin theorem, we have that

$$\mathbb{E} \left[\frac{|\mathcal{F}(\mathbf{x})[f_k]|^2}{n} \right] = \mathcal{F}(\mathbf{R})[f_k] \quad (30)$$

By construction, we have that $\mathcal{F}(\mathbf{R})[f_k] = S(f_k)$. This shows that in expectation, \mathbf{x} follows a power spectral density of $S(f_k)$. Lastly, because Σ is circulant, we have that the eigenvalues of Σ are the Discrete Fourier Transform of the first row, which is \mathbf{R} . As before, by construction, we have that $\mathcal{F}(\mathbf{R})[f_k] = S(f_k)$. From Equation (30), we have that the eigenvalues of Σ are precisely $c|f_k|^{-\beta}$. \square

Before we prove our main result, Theorem 2, we prove a useful lemma that calculates the posterior denoising distribution under a multivariate Gaussian assumption on the data.

Lemma 5. (Posterior Denoising Distribution) *Suppose $\mathbf{x}_0 \sim \mathcal{N}(\mathbf{0}, \Sigma)$. Suppose $\mathbf{x}_t | \mathbf{x}_0 \sim \mathcal{N}(\sqrt{\alpha_t}\mathbf{x}_0, (1 - \alpha_t)\mathbf{I})$. Then,*

$$p(\mathbf{x}_0 | \mathbf{x}_t) = \mathcal{N}(\boldsymbol{\mu}_{0|t}, \Sigma_{0|t}) \quad (31)$$

where $\boldsymbol{\mu}_{0|t} = \Gamma_t \mathbf{x}_t$, $\Gamma_t = \sqrt{\alpha_t} \Sigma (\alpha_t \Sigma + (1 - \alpha_t) \mathbf{I})^{-1}$, and $\Sigma_{0|t} = \Sigma - \sqrt{\alpha_t} \Gamma_t \Sigma$.

Proof. Suppose $\mathbf{x}_0 \sim \mathcal{N}(\mathbf{0}, \Sigma)$ and $\mathbf{x}_t | \mathbf{x}_0 \sim \mathcal{N}(\sqrt{\alpha_t}\mathbf{x}_0, (1 - \alpha_t)\mathbf{I})$. This implies that

$$\mathbf{x}_t = \sqrt{\alpha_t}\mathbf{x}_0 + (1 - \alpha_t)\boldsymbol{\epsilon} \quad (32)$$

where $\boldsymbol{\epsilon} \sim \mathcal{N}(\mathbf{0}, \mathbf{I})$. Therefore, we can write the joint distribution of \mathbf{x}_0 and \mathbf{x}_t as a multivariate Gaussian [2]:

$$\begin{bmatrix} \mathbf{x}_0 \\ \mathbf{x}_t \end{bmatrix} \sim \mathcal{N} \left(\mathbf{0}, \begin{bmatrix} \Sigma & \sqrt{\alpha_t}\Sigma \\ \sqrt{\alpha_t}\Sigma & \alpha_t\Sigma + (1 - \alpha_t)\mathbf{I} \end{bmatrix} \right). \quad (33)$$

Using properties of conditional Gaussian distributions, we have that $p(\mathbf{x}_0 | \mathbf{x}_t)$ is also a Gaussian distribution with conditional mean and covariance

$$\mathbb{E}[\mathbf{x}_0 | \mathbf{x}_t] = \sqrt{\alpha_t}\Sigma (\alpha_t\Sigma + (1 - \alpha_t)\mathbf{I})^{-1} \mathbf{x}_t \quad (34)$$

and

$$\text{Cov}[\mathbf{x}_0 | \mathbf{x}_t] = \Sigma - \sqrt{\alpha_t}\Sigma (\alpha_t\Sigma + (1 - \alpha_t)\mathbf{I})^{-1} \sqrt{\alpha_t}\Sigma. \quad (35)$$

Letting $\Gamma_t = \sqrt{\alpha_t}\Sigma (\alpha_t\Sigma + (1 - \alpha_t)\mathbf{I})^{-1}$, $\boldsymbol{\mu}_{0|t} = \mathbb{E}[\mathbf{x}_0 | \mathbf{x}_t]$ and $\Sigma_{0|t} = \text{Cov}[\mathbf{x}_0 | \mathbf{x}_t]$, we have shown the lemma. \square

Next, we prove our main theoretical result, Theorem 2, restated below.

Theorem 6. *Suppose \mathbf{x}_0 is drawn from $\mathcal{N}(\mathbf{0}, \Sigma)$ and we are given linear measurements $\mathbf{y} = \mathcal{A}(\mathbf{x}_0) + \mathbf{z}$, where $\mathcal{A}(\mathbf{x}_0) = \mathbf{A}\mathbf{x}_0$ and $\mathbf{z} \sim \mathcal{N}(0, \sigma_y^2\mathbf{I})$. Suppose that the intermediate value \mathbf{x}_t of the continuous-time reverse diffusion from Equation (5) can be written as $\mathbf{x}_t = \sqrt{\alpha_t}\mathbf{x}_0 + \sqrt{1 - \alpha_t}\boldsymbol{\epsilon}$ where $\boldsymbol{\epsilon} \sim \mathcal{N}(\mathbf{0}, \mathbf{I})$. Then, we have that*

$$\nabla_{\mathbf{x}_t} \log p(\mathbf{y} | \mathbf{x}_t) = (\mathbf{A}\Gamma_t)^T (\mathbf{A}\Sigma_{0|t}\mathbf{A}^T + \sigma_y^2\mathbf{I})^{-1} \boldsymbol{\Delta}_t, \quad (36)$$

where $\Gamma_t = \sqrt{\alpha_t}\Sigma (\alpha_t\Sigma + (1 - \alpha_t)\mathbf{I})^{-1}$, $\boldsymbol{\mu}_{0|t} = \mathbb{E}[\mathbf{x}_0 | \mathbf{x}_t] = \Gamma_t \mathbf{x}_t$, $\Sigma_{0|t} = \text{Cov}[\mathbf{x}_0 | \mathbf{x}_t] = \Sigma - \sqrt{\alpha_t}\Gamma_t \Sigma$, and $\boldsymbol{\Delta}_t = \mathbf{y} - \mathbf{A}\boldsymbol{\mu}_{0|t}$. Moreover, the approximation gap $\mathcal{J}^{DPS} := s^{DPS}(\mathbf{x}_t, \mathbf{y}) - s^*(\mathbf{x}_t, \mathbf{y})$ is given by:

$$\mathcal{J}^{DPS} = (\mathbf{A}\Gamma_t)^T (\sigma_y^{-2}\mathbf{I} - (\mathbf{A}\Sigma_{0|t}\mathbf{A}^T + \sigma_y^2\mathbf{I})^{-1}) \boldsymbol{\Delta}_t. \quad (37)$$

Proof. We denote $\hat{\mathbf{x}}_t$ as the iterate from the continuous-time reverse diffusion process such that $\hat{\mathbf{x}}_t = \sqrt{\alpha_t}\mathbf{x}_0 + \sqrt{1 - \alpha_t}\boldsymbol{\epsilon}$ where $\boldsymbol{\epsilon} \sim \mathcal{N}(\mathbf{0}, \mathbf{I})$. From Lemma 5, we have that $p(\mathbf{x}_0 | \hat{\mathbf{x}}_t) = \mathcal{N}(\boldsymbol{\mu}_{0|t}, \Sigma_{0|t})$ where $\boldsymbol{\mu}_{0|t} = \Gamma_t \hat{\mathbf{x}}_t$ and $\Sigma_{0|t} = \Sigma - \sqrt{\alpha_t}\Gamma_t \Sigma$. Now, similar to the proof of Lemma 5, since $p(\mathbf{y} | \mathbf{x}_0) = \mathcal{N}(\mathbf{A}\mathbf{x}_0, \sigma_y^2\mathbf{I})$, we can also calculate $p(\mathbf{y} | \hat{\mathbf{x}}_t)$ in closed form as another Gaussian distribution. Specifically, first we can write the joint distribution of \mathbf{x}_0 and \mathbf{y} conditioned on $\hat{\mathbf{x}}_t$ as a multivariate Gaussian [2]:

$$\begin{bmatrix} \mathbf{x}_0 \\ \mathbf{y} \end{bmatrix} \Big|_{\hat{\mathbf{x}}_t} \sim \mathcal{N} \left(\begin{bmatrix} \boldsymbol{\mu}_{0|t} \\ \mathbf{A}\boldsymbol{\mu}_{0|t} \end{bmatrix}, \begin{bmatrix} \Sigma_{0|t} & \Sigma_{0|t}\mathbf{A}^T \\ \mathbf{A}\Sigma_{0|t} & \mathbf{A}\Sigma_{0|t}\mathbf{A}^T + \sigma_y^2\mathbf{I} \end{bmatrix} \right). \quad (38)$$

Further, using properties of conditional Gaussian distributions, we have that $p(\mathbf{y} | \hat{\mathbf{x}}_t) = \mathcal{N}(\mathbf{A}\boldsymbol{\mu}_{0|t}, \mathbf{A}\Sigma_{0|t}\mathbf{A}^T + \sigma_y^2\mathbf{I})$. Let $\boldsymbol{\Delta}_t = \mathbf{y} - \mathbf{A}\boldsymbol{\mu}_{0|t}$. Then, computing the gradient

of $p(\mathbf{y} | \hat{\mathbf{x}}_t)$ with respect to $\hat{\mathbf{x}}_t$, we have

$$\nabla_{\hat{\mathbf{x}}_t} \log p(\mathbf{y} | \hat{\mathbf{x}}_t) = \nabla_{\hat{\mathbf{x}}_t} \log \mathcal{N}(\mathbf{A}\boldsymbol{\mu}_{0|t}, \mathbf{A}\boldsymbol{\Sigma}_{0|t}\mathbf{A}^T + \sigma_y^2\mathbf{I}) \quad (39)$$

$$= \nabla_{\hat{\mathbf{x}}_t} - 0.5\boldsymbol{\Delta}_t^T (\mathbf{A}\boldsymbol{\Sigma}_{0|t}\mathbf{A}^T + \sigma_y^2\mathbf{I})^{-1} \boldsymbol{\Delta}_t \quad (40)$$

$$= \left(\mathbf{A} \frac{\partial \boldsymbol{\mu}_{0|t}}{\partial \hat{\mathbf{x}}_t} \right)^T (\mathbf{A}\boldsymbol{\Sigma}_{0|t}\mathbf{A}^T + \sigma_y^2\mathbf{I})^{-1} \boldsymbol{\Delta}_t \quad (41)$$

As $\boldsymbol{\mu}_{0|t} = \boldsymbol{\Gamma}_t \hat{\mathbf{x}}_t$, we have that $\frac{\partial \boldsymbol{\mu}_{0|t}}{\partial \hat{\mathbf{x}}_t} = \boldsymbol{\Gamma}_t$, which gives us Equation (36). The DPS approximation to the true conditional score is $\nabla_{\hat{\mathbf{x}}_t} \log p(\mathbf{y} | \hat{\mathbf{x}}_t) \approx \nabla_{\hat{\mathbf{x}}_t} \log p(\mathbf{y} | \boldsymbol{\mu}_{0|t}) = \nabla_{\hat{\mathbf{x}}_t} \mathcal{N}(\mathbf{A}\boldsymbol{\mu}_{0|t}, \sigma_y^2\mathbf{I})$. Similar to above, we can also calculate its gradient with respect to $\hat{\mathbf{x}}_t$ as

$$\nabla_{\hat{\mathbf{x}}_t} \log p(\mathbf{y} | \boldsymbol{\mu}_{0|t}) = (\mathbf{A}\boldsymbol{\Gamma}_t)^T (\sigma_y^{-2}\mathbf{I}) \boldsymbol{\Delta}_t \quad (42)$$

The approximation gap \mathcal{J}^{DPS} is defined as

$$\mathcal{J}^{\text{DPS}} = s^{\text{DPS}}(\mathbf{x}_t, \mathbf{y}) - s^*(\mathbf{x}_t, \mathbf{y}) \quad (43)$$

$$= \nabla_{\hat{\mathbf{x}}_t} \log p(\mathbf{y} | \boldsymbol{\mu}_{0|t}) - \nabla_{\hat{\mathbf{x}}_t} \log p(\mathbf{y} | \mathbf{x}_t) \quad (44)$$

Note that in the second line, the unconditional score term cancels, so we are left only with the noisy likelihood difference. Subtracting Equation (36) from Equation (42), we have the approximation gap \mathcal{J}^{DPS} is equal to $(\mathbf{A}\boldsymbol{\Gamma}_t)^T (\sigma_y^{-2}\mathbf{I} - (\mathbf{A}\boldsymbol{\Sigma}_{0|t}\mathbf{A}^T + \sigma_y^2\mathbf{I})^{-1}) \boldsymbol{\Delta}_t$, completing our proof. \square

C. Further Motivations for our Method

In Section 4.1, we argued that when the forward operator is convolution with a high-pass filter, existing methods have a large approximation between the conditional score and its approximation, which can lead to compromised sample quality in practice. High-pass filtering may seem like a contrived example, because after all, many inverse problem tasks considered in the literature have forward operators that are low-pass filters, such as Gaussian deblurring and super-resolution tasks. However, for complex image restoration tasks such as motion deblurring, the forward operator can indeed act as a high-pass filter in certain spatial directions of the image. In Figure 6, we examine this effect by looking at the log magnitude of the frequency domain of an image convolved with a simple directional blur kernel. We can clearly see that in the red circled direction of the Fourier domain, the filter retains high frequency components of the original image. This is also mathematically evident using the Fourier convolution theorem. The Fourier convolution theorem states that

$$\mathcal{F}(k \otimes x) = \mathcal{F}(k) \cdot \mathcal{F}(x), \quad (45)$$

where \otimes denotes convolution and \cdot denotes an element-wise product. Further, for a directional blur kernel, the Fourier transform in spatial directions has high frequency values in directions orthogonal to the direction of the blur. Thus, it is clear that in those directions, the motion blur will retain high frequency components. While the high-pass filter considered in Figure 2 was an extreme case of this, our analysis highlights a crucial deficiency of existing methods since high frequency components of the measurement can amplify approximation errors.

D. Experimental Details

Below, we list the detailed setup for all experiments reported in the main paper. All the images for both FFHQ and ImageNet dataset are resized to 256×256 , and we report results for 1000 images from the validation datasets for the FFHQ and Imagenet datasets. We will release our code upon publication.

D.1. Inverse Problem Task Descriptions

D.1.1 Linear Inverse Problems

For the first three image restoration problems we consider, the forward operators are linear operators defined as convolution with a given kernel. These kernels are all of size 61×61 .

Gaussian Deblurring. The forward operator is convolution with a Gaussian blur kernel with standard deviation 3.

Motion Deblurring. The forward operator is convolution with a motion blur kernel generated from code¹ with intensity 0.5.

Deconvolution with High Pass Filter. the forward operator is a high-pass filter implemented as a Dirac kernel minus a Gaussian blur kernel of standard deviation 5.0.

D.1.2 Nonlinear Inverse Problems

Image Dehazing. The fourth image restoration is a nonlinear inverse problem, image dehazing, where the forward operator is a hazing operator with strength 1. The hazing operator models how light is scattered and attenuated in the atmosphere, based on the atmospheric scattering model

$$\mathcal{A}(\mathbf{x}) = \mathbf{x} \cdot t(\mathbf{x}) + L(1 - t(\mathbf{x})), \quad (46)$$

where \mathbf{x} is the original clear image (scene radiance), $t(\mathbf{x})$ is the transmission map representing the portion of light that reaches the camera, and L is the atmospheric light value. The transmission map $t(\mathbf{x})$ can be modeled using the Beer-Lambert law, which states that

$$t(\mathbf{x}) = e^{-\beta d(\mathbf{x})}. \quad (47)$$

¹<https://github.com/LeviBorodenko/motionblur>

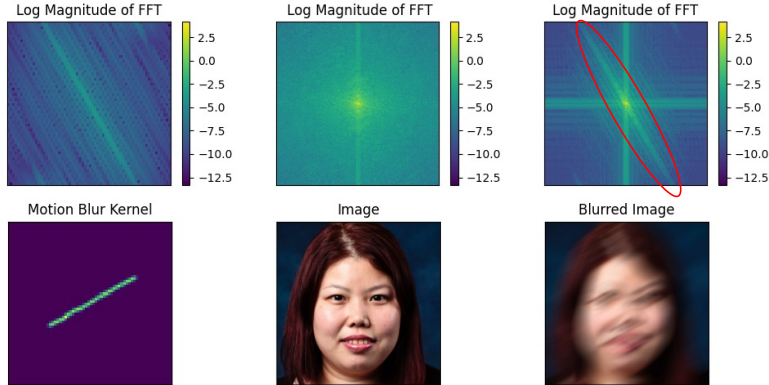


Figure 6. Directional motion blur can retain high frequency components in certain spatial directions orthogonal to the direction of the blur. The red circled direction shows an example of such a direction.

Above, β is the atmospheric scattering coefficient, and $d(\mathbf{x})$ is the scene depth map. In our experiments, we set $L = 1$, $\beta = 1$, and set $d(\mathbf{x})$ be Euclidean distance of each pixel to the center of the image.

D.2. Baselines

DPS [9] We use the code from <https://github.com/DPS2022/diffusion-posterior-sampling> using the default hyperparameter settings for Gaussian deblurring and motion deblurring for both FFHQ and ImageNet. For high-pass filter operator, we used the same hyperparameters used for motion deblurring.

MCG [10] We use the code from https://github.com/HJ-harry/MCG_diffusion using the default hyperparameter settings for Gaussian deblurring and motion deblurring for both FFHQ and ImageNet. For high-pass filter operator, we used the same hyperparameters used for motion deblurring.

DSG [41] We use the code from <https://github.com/LingxiaoYang2023/DSG2024> using the default hyperparameter settings for Gaussian deblurring for both FFHQ and ImageNet. The only hyperparameter change was that we set $interval = 10$ as we observed this worked better in practice. For high-pass filter deconvolution and motion deblurring operator, we used the same hyperparameters used for Gaussian deblurring.

Score-SDE/ILVR [8, 35] Generally, we group Score-SDE and ILVR as methods that use a sequence of noisy measurements to approximate the conditional score, as mentioned in [12] and [9]. This is a generalization of the methods in [35] and [8] as their methods only were presented for the inpainting and superresolution tasks. To consider general tasks, we sample a sequence of measurements $\mathbf{y}_t \sim \mathcal{N}(\sqrt{\alpha_t}\mathbf{y}, (1 - \alpha_t)\mathbf{I})$. Then, we approximate the con-

ditional score as $-\eta \nabla_{\mathbf{x}_t} \|\mathbf{y}_t - \mathcal{A}(\mathbf{x}_t)\|_2^2$. We use the step size η from the DPS method [9].

AOD-Net. We use the code from <https://github.com/MayankSingal/PyTorch-Image-Dehazing> and train the network using the default parameters on 10000 images from the FFHQ training dataset.

DoubleDIP. We use the code from <https://github.com/yossigandelman/DoubleDIP> using all default parameters. This method is unsupervised and does not require any retraining.

D.3. Details for Figure 2 and Figure 3

In Figure 2 and Figure 3, we demonstrated the approximation gap of DPS and our method on synthetic data. Below, we describe the precise experimental details of our experiments.

Forward Operators. We consider two operators in our experiments: a low-pass filter and a high-pass filter. For the low-pass filter, we create a circulant matrix \mathbf{A}_l whose first row is a Gaussian blur kernel of width σ i.e. this kernel is $e^{-\mathbf{x}^2/(2\sigma^2)}$ and normalized to have sum 1. Multiplying \mathbf{A}_l with a signal \mathbf{x} corresponds to convolving \mathbf{x} with the Gaussian blur kernel. In our experiments, we vary σ as shown as the different lines in the figures. For the high-pass filter, we simply subtract the Gaussian blur kernel of width σ from a Dirac kernel, which has 1 at the center and zeroes elsewhere. Importantly, the first row of the circulant matrix corresponding to this kernel is normalized to have sum zero, such that the kernel is indeed a high-pass filter.

Data Generation. Next, we describe the data generation process. Recall from Lemma 1 the construction of a covariance matrix Σ_f such that data drawn from $\mathcal{N}(\mathbf{0}, \Sigma_f)$ follows a power law in the frequency domain with parameters c and β . We let $c = 1$ and $\beta = 2.5$, which is the typical

range for natural image data [38]. We draw 10000 signals $\mathbf{x}^{(i)}$ of length 2000 from $\mathcal{N}(\mathbf{0}, \Sigma_f)$. For each signal, we generate a corresponding measurement $\mathbf{y}^{(i)} = \mathbf{A}\mathbf{x}^{(i)} + \mathbf{z}$, where $\mathbf{z} \sim \mathcal{N}(\mathbf{0}, \mathbf{I})$, and \mathbf{A} is the circulant matrix corresponding to the low-pass filter or the high-pass filter.

Approximation Gap. For each $\mathbf{x}^{(i)}, \mathbf{y}^{(i)}$ pair, we calculate $\mathbf{x}_t^{(i)} \sim \mathcal{N}(\sqrt{\bar{\alpha}_t}\mathbf{x}^{(i)}, (1 - \bar{\alpha}_t)\mathbf{I})$, where $\bar{\alpha}_t$ is the variance schedule from the DDPM paper [20]. We report the average approximation gap over the 10000 signals.

Frequency Curriculum. For our method, we have the choices of the frequency curriculum described through τ_T and τ_1 , the frequency cutoffs for the time-dependent low pass filter. For simplicity, we use a frequency curriculum from the variance schedule of the diffusion model. Specifically, let $\sigma_t = \frac{1}{\bar{\alpha}_t} - 1$, which corresponds to the corresponding variance-exploding parameterization of the SDE (see [24], Appendix B). Then we set τ_t be the max frequency value f_k such that $S(f_k) \geq \max\{\sigma_y^2, \sigma_t^2\}$, where $S(f_k)$ denotes the power spectral density from Equation (8). This utilizes the intuition that for $\mathbf{x}_t^{(i)}$, the frequency components of the original signal $\mathbf{x}^{(i)}$ still present in the image are the frequencies below τ_t .

D.4. Implementation Details for Our Method

In practice, we let τ_1 and τ_T be hyperparameters and consider various schedules to interpolate between them. However, our theoretical results can guide us on setting them in a data-dependent way. Recall that natural images tend to follow a radially averaged power law in the frequency domain such that each non-zero frequency f_k has power $S(f_k) \approx c|f_k|^{-\beta}$ for some constants $c, \beta > 0$. We employ three heuristics for setting our frequency schedule.

1. (Setting τ_1 to improve robustness to noise) When the measurement noise has variance σ_y^2 , higher frequency components of \mathbf{y} are affected, specifically those frequencies f such that $S(f) \leq \sigma_y^2$. Denoting f_{noise} as the minimum frequency value that satisfies this constraint, we can set τ_1 less than f_{noise} and make our method robust to additive Gaussian noise of a known variance.
2. (Frequency Schedule as Function of Power Law Decay) For data that follows a faster decaying power law (when β is larger), we can set a schedule for τ_t that also increases faster as a function of t .
3. (Setting τ_T) For natural images, it is sufficient to set τ_T to be a small percentage of the overall frequency range, as this contains most of the information present in the measurement \mathbf{y} . This is the same intuition behind JPEG compression. In our experiments on natural images, we take τ_T to be roughly 30% of the overall frequency range.

To implement a frequency schedule, we use a binary

mask applied in the frequency domain. Specifically, we utilize the Fast Fourier Transform (FFT) to transform the image data into the frequency domain. A low-pass filter mask is then created based on a specified cutoff frequency τ_t . We utilize the Euclidean distance from the center of the frequency domain to create the low-pass filter mask, which selectively retains frequencies below the cutoff value. As the reverse process progresses, the cutoff is adjusted to allow more high-frequency components, thereby refining the image details. This method efficiently integrates frequency control into the reverse diffusion process, contributing to improved image restoration. In our work, we consider two frequency schedules, an exponential schedule and a linear schedule, which interpolate between τ_T and τ_1 in different ways. Precisely, the exponential schedule follows

$$\tau_t = \tau_1 - (\tau_1 - \tau_T) \exp\left(-\frac{5t}{T}\right), \quad (48)$$

and the linear schedule follows

$$\tau_t = \tau_T + \frac{t}{T}(\tau_1 - \tau_T). \quad (49)$$

Further, we set the step size \mathbf{S}_t to be $\mathbf{S}_t = \frac{\kappa_t}{\|\phi_t(\mathbf{y}) - \phi(\mathcal{A}(\mu_{0|t}))\|_2} \mathbf{I}$ for a scalar time-dependent hyperparameter κ_t . We set this schedule to smoothly transition from κ_T at the beginning of the reverse process to κ_1 at the end. Precisely, this schedule follows

$$\kappa_t = \frac{1}{2}(\kappa_T + \kappa_1) + \frac{1}{2}(\kappa_T - \kappa_1) \cos\left(\frac{\pi t}{T}\right), \quad (50)$$

where t denotes the current time step, and T is the total number of time steps (e.g. 1000 in our case).

Next, we detail all the hyperparameter settings used for our experiments on the FFHQ and ImageNet datasets.

- FFHQ
 - Gaussian Deblurring:
 - * Step Size: $\kappa_T = 3.0, \kappa_1 = 0.6$
 - * Frequency Schedule: Exponential
 - Motion Deblurring:
 - * Step Size: $\kappa_T = 5.0, \kappa_1 = 1.0$
 - * Frequency Schedule: Exponential
 - High pass:
 - * Step Size: $\kappa_T = 5.1, \kappa_1 = 1.1$
 - * Frequency Schedule: Linear
 - Haze:
 - * Step Size: $\kappa_T = 5.0, \kappa_1 = 1.0$
 - * Frequency Schedule: Exponential
- ImageNet
 - Gaussian Deblurring:
 - * Step Size: $\kappa_T = 2.0, \kappa_1 = 0.01$
 - * Frequency Schedule: Linear

- Motion Deblurring:
 - * Step Size: $\kappa_T = 3.0, \kappa_1 = 0.1$
 - * Frequency Schedule: Linear
- High pass:
 - * Step Size: $\kappa_T = 3.5, \kappa_1 = 0.6$
 - * Frequency Schedule: Linear

In Appendix F, we provide ablation studies to understand the effects of these hyperparameters on the generation quality.

D.5. Computational Overhead of Our Method

In this section, we evaluate the computational efficiency of our method by measuring the average runtime per image on the FFHQ dataset. We run each method from Table 1 on 100 images, and report the average time taken per image, given in Table 3. We see that our method introduces minimal computational overhead compared to the DPS method, demonstrating that our modifications can be implemented in an efficient manner and easily integrated into existing frameworks.

Method	Time (seconds)
DSG	45.13744
Score-SDE/ILVR	41.411510
MCG	93.20647
DPS	90.641704
FPGS (Ours)	92.383272

Table 3. Average Wall Clock Runtime Per Image (seconds) on FFHQ Dataset

E. Comparison to ILVR/Score-SDE

Our method is closely related to the Score-SDE and ILVR works that consider a sequence of noisy measurements y_t such that $y_t = \mathcal{N}(\sqrt{\alpha_t}y_0, (1 - \alpha)\mathbf{I})$ [8, 35]. These methods consider approximations to the noisy likelihood score that are typically of the form $\mathbf{L}_A(\mathbf{y}_t - \mathcal{A}(\mathbf{x}_t))$, where \mathbf{L}_A is a fixed matrix that depends on the measurement operator \mathcal{A} . There are three crucial differences between these methods and our method. First, our approximation to the noisy likelihood score considers a time-varying model likelihood at each diffusion timestep $p(\mathbf{y} | \boldsymbol{\mu}_{0|t})$ as given in Equation (13) as opposed to simply varying \mathbf{y}_t . Further, we leverage the powerful denoising capabilities of the pre-trained diffusion model by using the Tweedie estimate $\boldsymbol{\mu}_{0|t}$ instead of the noisy \mathbf{x}_t . Lastly, we propose a frequency curriculum that can differ from the variance schedule of the diffusion model and be adapted to the frequency characteristics of the data. These differences lead to a drastically improved performance of our method compared to Score-SDE/ILVR as seen in Table 1.

F. Further Experiments and Ablation Studies

F.1. Visualizing the Transformed Measurements

In Figure 7, we show the transformed measurements at three timesteps in the reverse diffusion process when applying our frequency curriculum on the FFHQ dataset. As we can see, in the early stages of the reverse process, the measurement retains only a coarse outline of the measurement. Our theoretical results indicate that the initial reverse process steps are very important in order to obtain coarse alignment with the given measurement.

F.2. Effect of Frequency Curriculum

Impact of Time-Dependent Curriculum. As observed in Figure 5, we observe that the time-dependent frequency curriculum helps the stability of the method. Namely, when the operator is a high pass filter, the time-dependent frequency curriculum results in high-quality reconstructions. On the other hand, for a fixed curriculum, we observe that over different generations, most random samples of the diffusion model fall off the natural image manifold in the early steps of the reverse process, which results in unnatural looking images as in Figure 5.

Next, to assess the impact of different frequency curricula on image quality, we provide a visual comparison using images generated with linear and exponential time-dependent curricula on the FFHQ and ImageNet datasets.

FFHQ Motion Deblurring. The images produced with the exponential frequency schedule exhibit superior quality, as shown in Figure 9. The exponential increase in high-frequency components helps to better capture fine facial features and intricate details, resulting in more visually appealing images.

ImageNet Motion Deblurring. The ImageNet dataset benefits more from the linear frequency schedule, as illustrated in Figure 10. We hypothesize this is because the diversity and detail of ImageNet scenes require more careful consideration at many frequency ranges to obtain a high-quality reconstruction.

Motivation for Frequency Schedule Selection. Our observations indicate that the choice of frequency schedule should be informed by the characteristics of the underlying data. The exponential schedule is well-suited for datasets with structured and hierarchical features, such as faces, where it is crucial to refine high-frequency details over an extended number of reverse process time steps. In contrast, datasets like ImageNet, which contain diverse and complex textures, benefit from a more uniform and gradual frequency progression, ensuring consistent detail incorporation throughout the sampling process. We note though that while our method offers the flexibility to incorporate

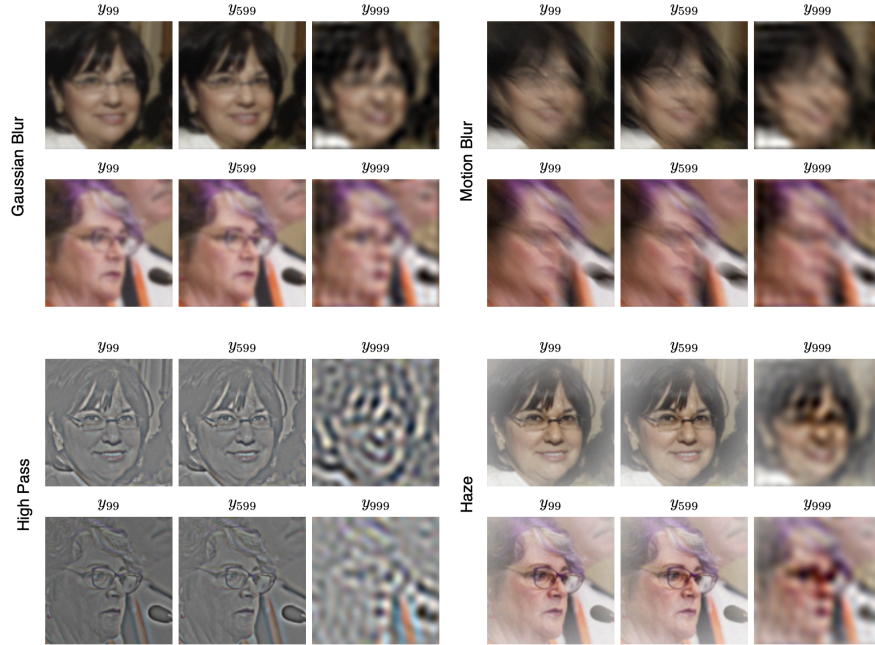


Figure 7. We demonstrate the visual effects of our frequency curriculum on the transformed measurements. In the early stages of the reverse process, only very coarse features of the measurement are retained.



Figure 8. Qualitative comparison of different scale schedules on the FFHQ dataset. The first row highlights how the cosine schedule accurately captures details, such as the necklace, while the fixed small step size ($\kappa = 1$) fails and the fixed large step size ($\kappa = 5$) introduces artifacts.

different frequency curricula, it is not a necessity to obtain high-quality reconstructions, and even a simple exponential curriculum can already obtain results that are significantly better than baseline methods. We simply highlight that this can be further improved by carefully considering the frequency distribution of the data.

F.3. Effect of Step Size Schedule

Recall that in Equation (15), we had that our approximation to the score should be scaled by S_t , which can be thought of as a step size to the gradient term. In practice, instead of using this exact quantity, which would require using a potentially large circulant matrix and its inverse, we

set $\mathbf{S}_t = \frac{\kappa}{\|\phi_t(\mathbf{y}) - \phi(\mathcal{A}(\mu_{0:t}))\|_2} \mathbf{I}$ for a scalar hyperparameter κ , which works well in practice. This is similar to the step size chosen in DPS. The intuition behind this step size choice is to control the approximation error. For example, when the approximation error is high, the step size should be smaller as the conditional score is noisy. These schedules play a crucial role in the effectiveness and stability of the optimization process. In this section, we study the effect of different step size schedules to motivate our choice. Specifically, we study three step size schedules (where we vary κ) on the motion deblurring task on the FFHQ dataset. These three schedules are:

1. Fixed small step size (used by DPS)
2. Fixed large step size
3. Cosine Annealed step size according to Equation (50).
This schedule starts with a relatively high step size, which facilitates rapid progress in the initial stages, and gradually decreases to smaller step sizes as the optimization nears convergence.

In Table 4 and Figure 8, we demonstrate the quantitative and qualitative differences between the three schedules. We clearly see that the cosine annealed step size strongly outperforms the other two schedules, which is why we adopt it for our experiments. We hypothesize that the cosine schedule allows the model to quickly capture the coarse structure of the image early on, while the progressively smaller steps enable fine-tuning of details, leading to a more refined final reconstruction. This is evident from Figure 8. For example, in the first row, the cosine schedule successfully captures the necklace detail around the subject’s neck, while the fixed small step size schedule completely misses this feature, resulting in a blurred and oversmoothed output. The fixed large step size schedule manages to retain some necklace details but introduces noticeable artifacts, which degrade the overall image quality. The large step size likely destabilizes the optimization and pushes the image off the natural image manifold, which compromises image quality.

Step Size Schedule	FID↓	LPIPS↓	PSNR↑	SSIM↑
Cosine Annealing	49.66	0.1254	25.53	0.724
Fixed Lower Bound	70.73	0.1790	24.22	0.677
Fixed Upper Bound	59.94	0.1559	24.22	0.686

Table 4. Performance comparison of different scale schedules on the FFHQ dataset. Metrics include FID, LPIPS, PSNR, and SSIM.

F.4. Further Qualitative Results

Comparison to Baselines. In Figure 11, we see the zoomed in version from Figure 4, highlighting the intricate details of the image captured by our reconstructions. In Figure 12, we see a comprehensive comparison to all the baselines re-

ported in Table 1 on the motion blurring task on the FFHQ dataset. We observe that Score-SDE/ILVR often captures the correct structure of the image but fills in different facial features. MCG usually overfits to the Gaussian measurement noise as reported in [9]. DPS results in good quality reconstructions, but the images are usually smoothed out and lose small facial features. DSG performs very well on the motion deblurring task, as shown also in Table 1. However, DSG often gives grainy reconstructions and artifacts that are clearly visible. In contrast, our method is significantly more stable and is able to give images that have higher perceptual quality than all the baselines.

FFHQ Additional Results. Figures 13 and 14 show additional results of our method on the motion deblurring and image dehazing task on the FFHQ dataset.

ImageNet Additional Results. Figures 15, 16, and 17 show additional results of our method on the Gaussian deblurring, motion deblurring, and high-pass filter deconvolution tasks on the ImageNet dataset. On the high-pass filter task, we note that there is sometimes a color shift which results from the loss of color information in the measurement. We observe that compared to DPS and a fixed-time frequency curriculum (as in Figure 5), our method is much more stable and usually gives visually plausible reconstructions instead of strong color artifacts that dominate the reconstruction.

G. Limitations and Future Work

While FGPS requires little frequency schedule tuning, the step size still plays a large role in dictating image quality and needs to be carefully tuned. Further, the frequency curriculum is applicable only for image restoration tasks where the measurement is still an image. Lastly, similar to DPS, FGPS requires knowledge of the forward operator during the reverse process, which restricts it to non-blind inverse problems.

Future work would include a rigorous analysis of the step size and how it affects the approximation error. It would also be useful to consider several competing works and their introduced approximation errors using our theoretical analysis as a backbone. Lastly, we hope to extend FGPS to other inverse problems, both blind and non-blind, where the measurement is not an image such as medical imaging tasks.

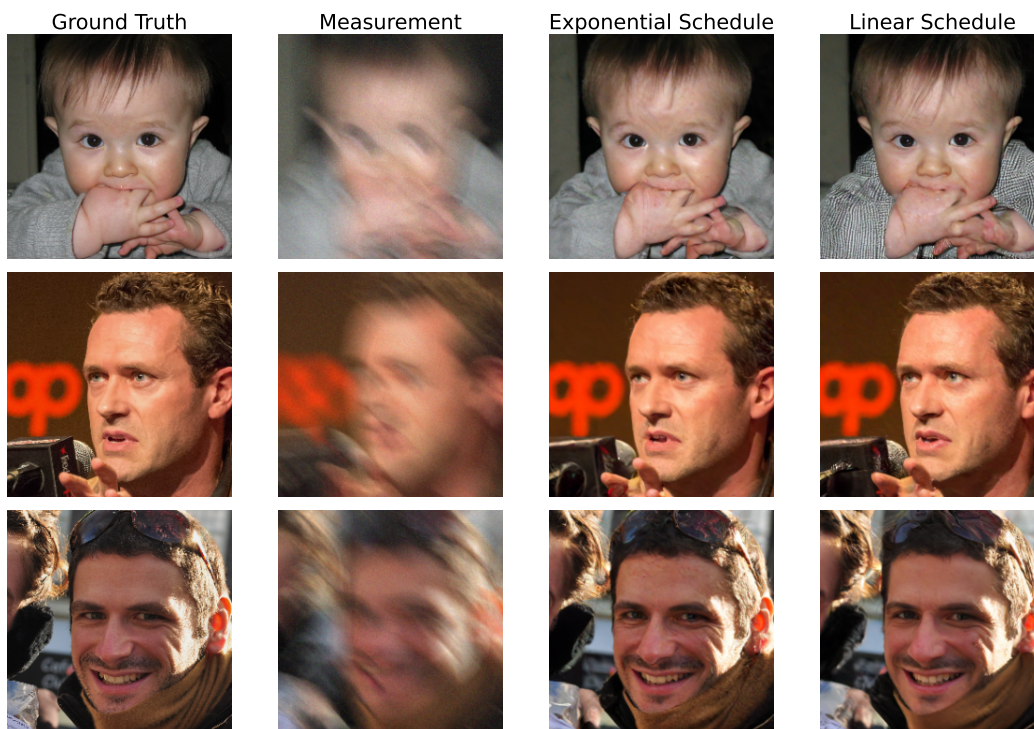


Figure 9. Comparison of images on the FFHQ dataset using exponential and linear frequency schedules. The exponential schedule produces higher-quality images with refined details and realistic textures compared to the linear schedule.

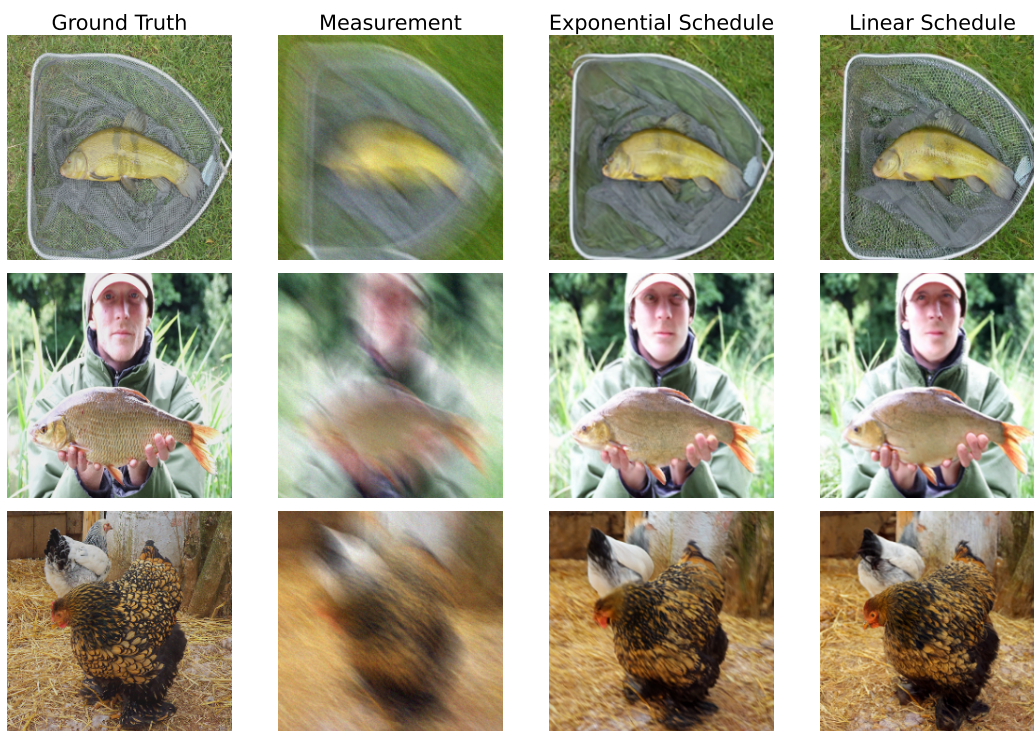


Figure 10. Comparison of images on the ImageNet dataset using exponential and linear frequency schedules. The linear schedule preserves object shapes and structural details better, resulting in clearer images.



Figure 11. Qualitative results of our method with zoomed in portions of images from Figure 4. Our method successfully preserves finer details like background pattern.



Figure 12. Qualitative motion deblurring results on FFHQ dataset for all baselines we report in Table 1. The same blur kernel is applied to each image.

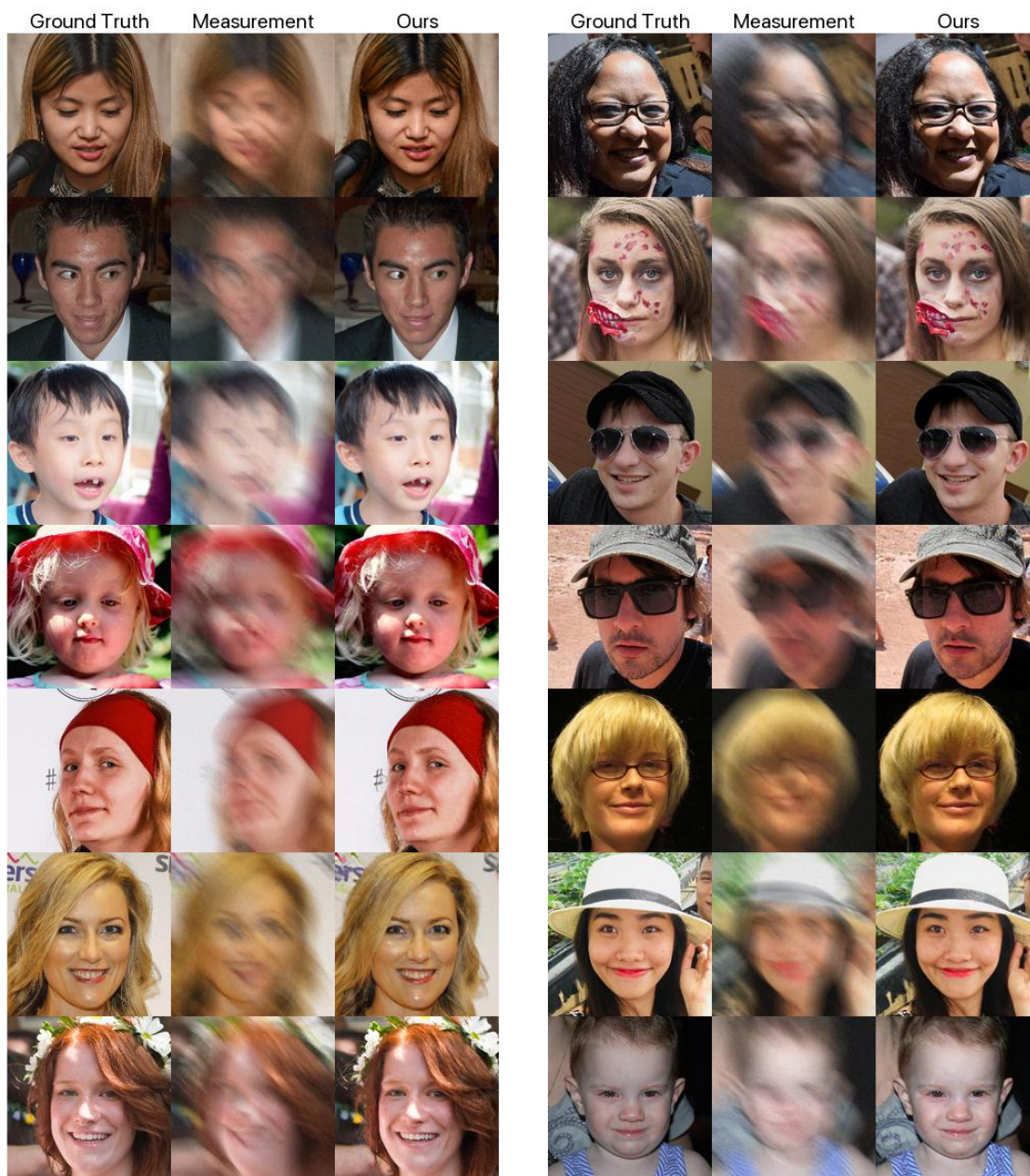


Figure 13. Qualitative motion deblurring results on FFHQ dataset. The same blur kernel is applied to each image.

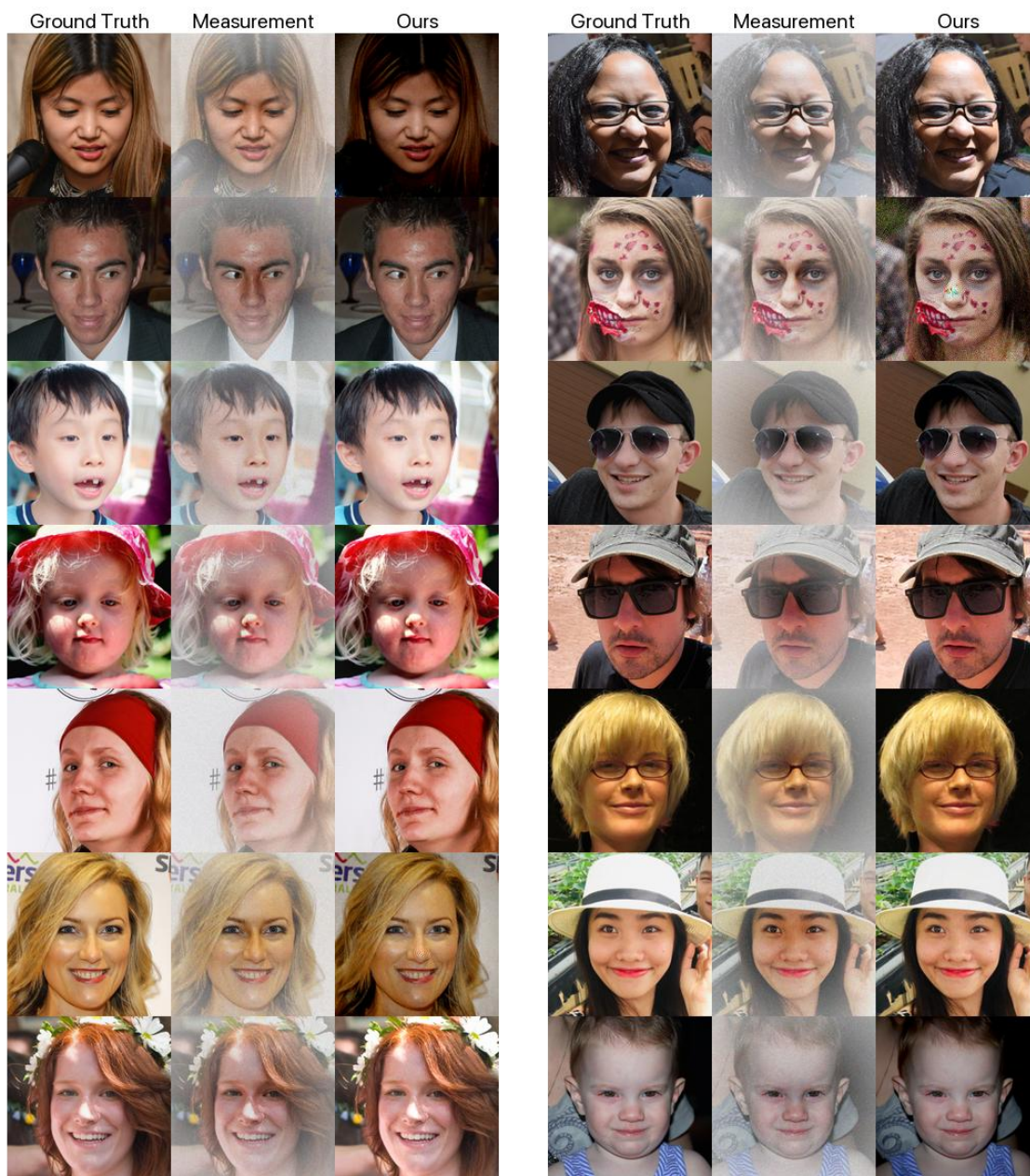


Figure 14. Qualitative image dehazing results on FFHQ dataset.



Figure 15. Qualitative Gaussian deblurring results on Imagenet dataset.

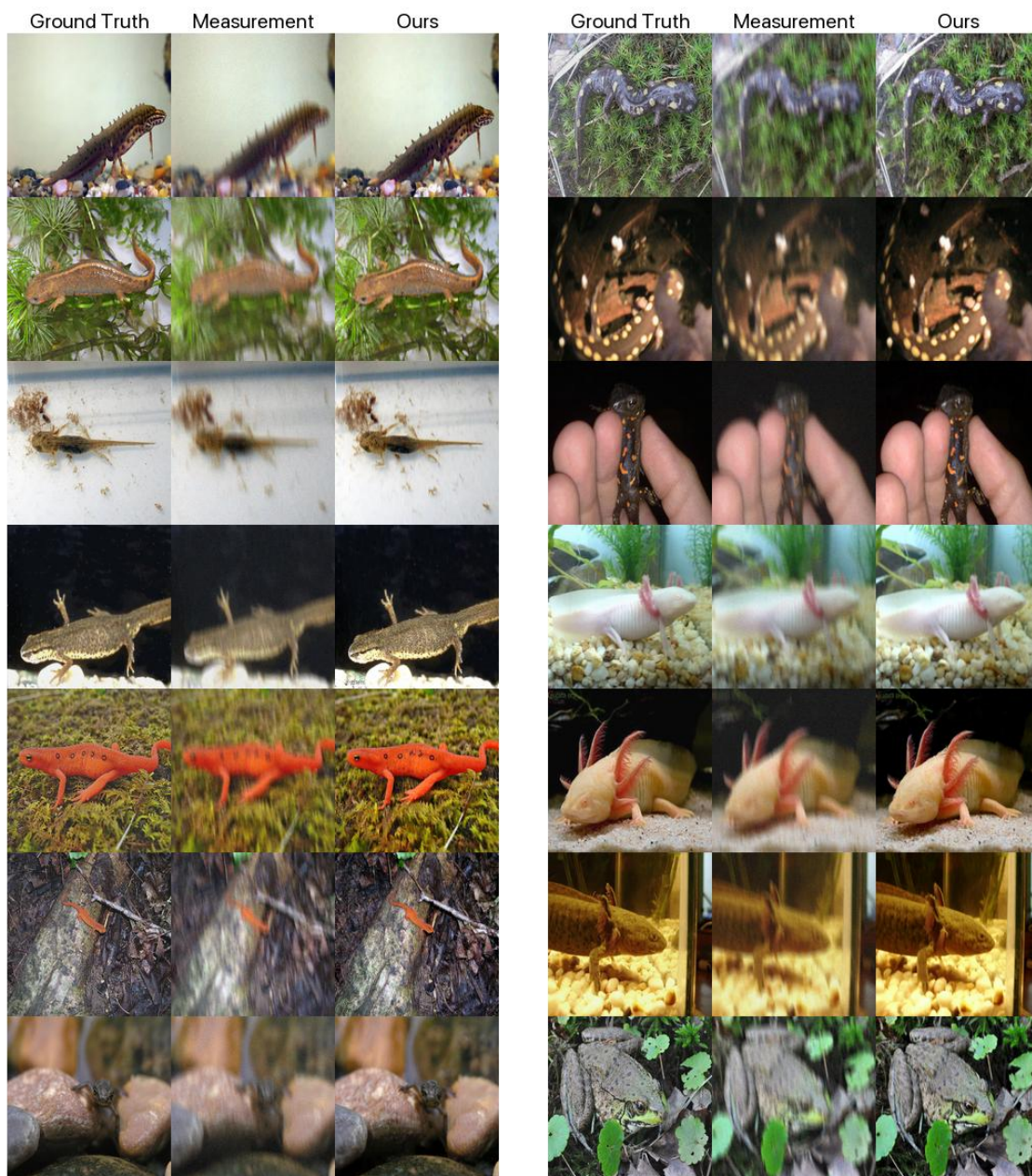


Figure 16. Qualitative motion deblurring results on Imagenet dataset. The same blur kernel is applied to each image.

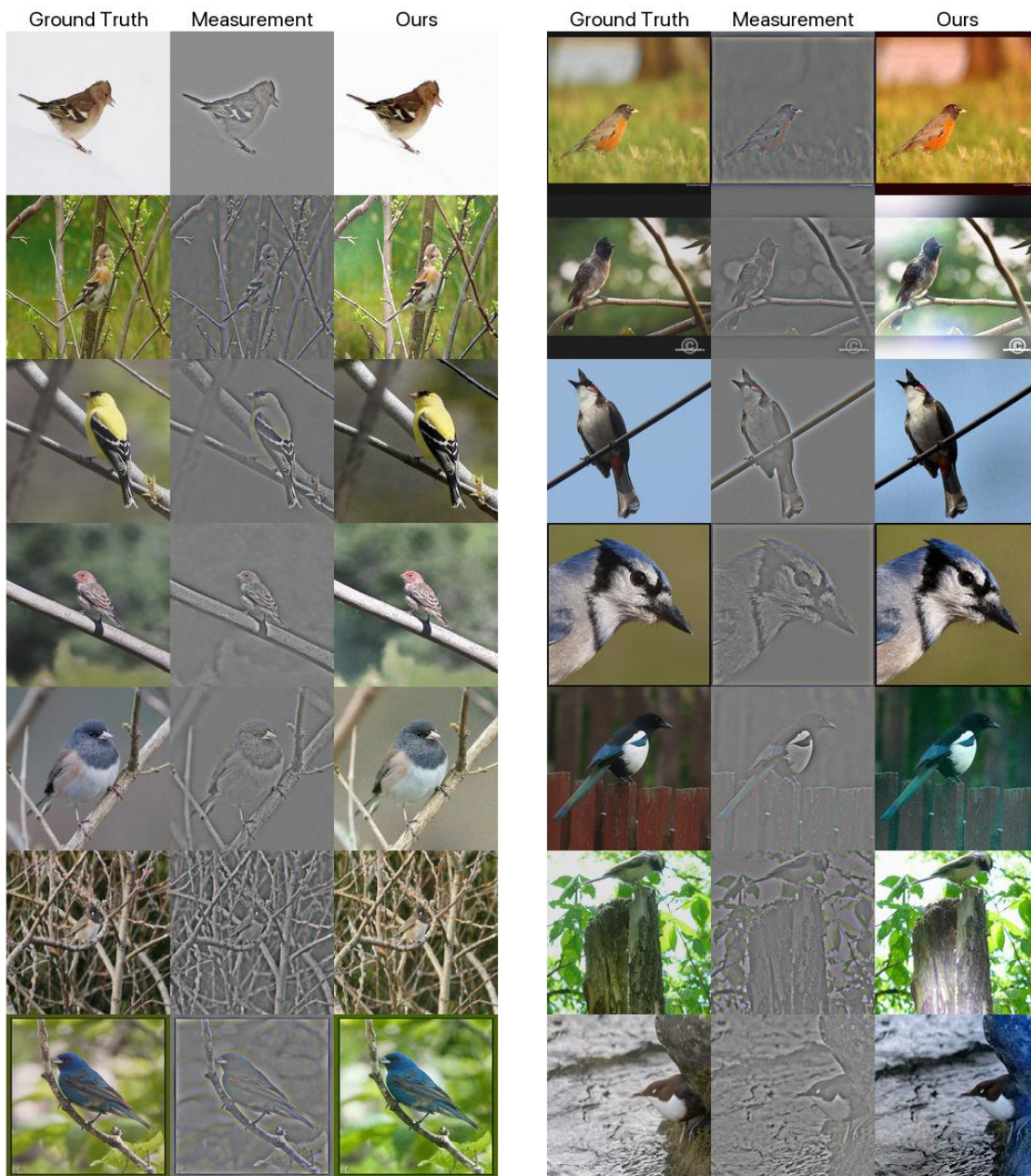


Figure 17. Qualitative results on Imagenet dataset when the measurement is a high-pass filter applied to the ground truth image.